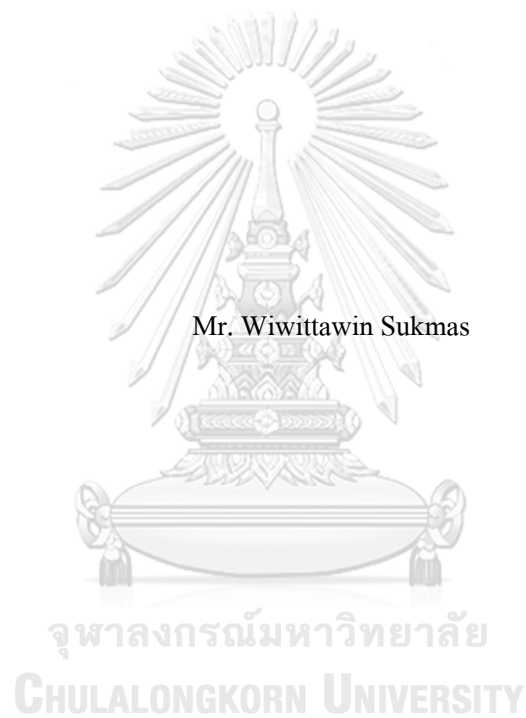


AB INITIO CALCULATIONS ON SUPERCONDUCTING METAL-HYDRIDE AND
PEROVSKITES FOR ENERGY APPLICATIONS



A Dissertation Submitted in Partial Fulfillment of the Requirements

for the Degree of Doctor of Philosophy in Physics

Department of Physics

FACULTY OF SCIENCE

Chulalongkorn University

Academic Year 2021

Copyright of Chulalongkorn University

การคำนวณแบบแอนิซิโอในตัวยังขวดโลหะไฮไดรด์และเพอร์อฟสไกต์สำหรับการ
ประยุกต์ใช้เชิงพลังงาน



วิทยานิพนธ์นี้เป็นส่วนหนึ่งของการศึกษาตามหลักสูตรปริญญาวิทยาศาสตรดุษฎีบัณฑิต
สาขาวิชาฟิสิกส์ ภาควิชาฟิสิกส์
คณะวิทยาศาสตร์ จุฬาลงกรณ์มหาวิทยาลัย
ปีการศึกษา 2564
ลิขสิทธิ์ของจุฬาลงกรณ์มหาวิทยาลัย

Thesis Title AB INITIO CALCULATIONS ON SUPERCONDUCTING
METAL-HYDRIDE AND PEROVSKITES FOR ENERGY
APPLICATIONS
By Mr. Wiwittawin Sukmas
Field of Study Physics
Thesis Advisor Associate Professor THITI BOVORN RATANARAKS, Ph.D.
Thesis Co Advisor Associate Professor UDOMSILP PINSOOK, Ph.D.

Accepted by the FACULTY OF SCIENCE, Chulalongkorn University in Partial
Fulfillment of the Requirement for the Doctor of Philosophy

..... Dean of the FACULTY OF SCIENCE
(Professor POLKIT SANGVANICH, Ph.D.)

DISSERTATION COMMITTEE

..... Chairman
(Associate Professor Sutee Boonchui, Ph.D.)

..... Thesis Advisor
(Associate Professor THITI BOVORN RATANARAKS, Ph.D.)

..... Thesis Co-Advisor
(Associate Professor UDOMSILP PINSOOK, Ph.D.)

..... Examiner
(Assistant Professor THITI TAYCHATANAPAT, Ph.D.)

..... Examiner
(Assistant Professor RANGSIMA CHANPHANA, Ph.D.)

..... Examiner
(CHAYANIT ASAWATANGTRAKULDEE, Ph.D.)

วิจิตรวิทย์ สุขมาศ : การคำนวณแบบแอบอินิซิโอในตัวนำยิ่งยวดโลหะไฮไดรด์และเพอโรฟสไกต์สำหรับการประยุกต์ใช้เชิงพลังงาน. (AB INITIO CALCULATIONS ON SUPERCONDUCTING METAL-HYDRIDE AND PEROVSKITES FOR ENERGY APPLICATIONS) อ.ที่ปรึกษาหลัก : รศ. ดร.ธิดา บวรรัตนารักษ์, อ.ที่ปรึกษาร่วม : รศ. ดร.อุดมศิลป์ ปิ่นสุข

การประยุกต์เชิงพลังงานของตัวนำยิ่งยวดโลหะไฮไดรด์และวัสดุเซลล์สุริยะเพอโรฟสไกต์ถูกนำมาศึกษาผ่านกระบวนการคำนวณเชิงควอนตัมที่มีพื้นฐานมาจากทฤษฎีฟังก์ชันความหนาแน่น (DFT) ผลการคำนวณพบว่าสารประกอบอัลลอยด์สูตร $Mg_{0.5}Ca_{0.5}H_6$ มีความเสถียรเชิงอุณหพลศาสตร์ภายใต้ความดันในช่วง 200 ถึง 400 GPa เท่านั้น และสมบัติเชิงอิเล็กทรอนิกส์ของสารประกอบนี้ได้ส่งสัญญาณถึงความเป็นไปได้ที่สารนี้จะเป็นตัวนำยิ่งยวดภายใต้ความดันสูง ซึ่งผลที่ได้จากการคำนวณ electron-phonon coupling พบว่าค่าอุณหภูมิวิกฤตของสารประกอบ $Mg_{0.5}Ca_{0.5}H_6$ มีค่าสูงถึง 288 K ที่ความดัน 200 GPa ส่วนต่อมาการคำนวณโดยรวมผลของอันตรกิริยา van de Waals ได้ถูกนำไปใช้เพื่อการศึกษาการวางตัวของโมเลกุลอินทรีย์ CH_3NH_3 (MA) ในเพอโรฟสไกต์ $MAPbI_3$ ฟังก์ชัน vdW-DF-cx ได้ถูกเลือกเพื่อคำนวณหาพลังงานของระบบที่มีรูปแบบการเรียงตัวที่แตกต่างกันของโมเลกุล MA ภายใต้ความดัน และส่วนสุดท้ายนี้ได้มีการประยุกต์ใช้มอดูลอร์ในการศึกษาการหมุนในสามมิติของโมเลกุลอินทรีย์ MA ภายในเพอโรฟสไกต์ที่ปราศจากสารตะกั่วอย่าง $MABiSe_2$ ซึ่งได้แสดงถึงภูมิทัศน์เชิงพลังงานของระบบนี้ ทั้งนี้การจำลองเชิงสถิติที่ใช้พื้นฐานของ deep learning ได้ถูกออกแบบขึ้นเพื่อทำนายพลังงานรวมของระบบที่ได้จากการวางตัวของโมเลกุล MA ทำให้ลดการคำนวณที่ใช้ทรัพยากรสูงอย่าง DFT ได้

สาขาวิชา ฟิสิกส์
ปีการศึกษา 2564

ลายมือชื่อนิสิต
ลายมือชื่อ อ.ที่ปรึกษาหลัก
ลายมือชื่อ อ.ที่ปรึกษาร่วม

6271035623 : MAJOR PHYSICS

KEYWORD:

Wiwittawin Sukmas : AB INITIO CALCULATIONS ON SUPERCONDUCTING METAL-HYDRIDE AND PEROVSKITES FOR ENERGY APPLICATIONS.

Advisor: Assoc. Prof. THITI BOVORN RATANARAKS, Ph.D. Co-advisor: Assoc. Prof. UDOMSILP PINSOOK, Ph.D.

Superconducting hydrides and photovoltaic perovskites for energy applications are studied by means of the density functional theory-based calculations. First of all, the new decoration of $\text{Mg}_{0.5}\text{Ca}_{0.5}\text{H}_6$ is confirmed thermodynamically stable over the pressures ranging from 200 to 400 GPa. The electronic properties reveal the possibility for this very material of becoming a superconductor under pressures. As a result, by performing electron-phonon coupling (EPC) calculations, $\text{Mg}_{0.5}\text{Ca}_{0.5}\text{H}_6$ is found to superconduct at a maximum critical temperature of 288 K at 200 GPa, which completely exceeds those of its parent compounds, i.e. MgH_6 and CaH_6 . Secondly, the van de Waals (vdW) interaction is incorporated in the DFT calculations to determine the preferred orientations of the organic CH_3NH_3 (MA) cation embedded at the centre of MAPbI_3 perovskite. The well-developed vdW-DF-cx functional is selected to evaluate the total energies of different MA dipolar configurations in a cubic supercell of MAPI under pressures. Finally, due to its lead-free contents, MABiSe_2 perovskite is applied the Eulerian angles to its MA cation in three-dimensional space to determine its corresponding total energies. The complexity of angle-energy relationship is alleviated with the help of a high-fidelity simulation based on deep learning.

Field of Study: Physics

Academic Year: 2021

Student's Signature

Advisor's Signature

Co-advisor's Signature

ACKNOWLEDGEMENTS

I would like to express the deepest appreciation to the best supervisor ever, Assoc Prof Thiti Bovornratanaraks, Ph.D, and my co-advisor Assoc Prof Udomsilp Pinsook, Ph.D, who gave me the golden opportunity to do these marvellous projects that also helped me in doing a lot of research and I came to know about so many new things I am really grateful of them. Without their guidance and persistent help this thesis would not have been possible. I would like to also offer my gratitude to Dr Prutthipong Tsuppayakorn-aeek for his role in making me master many computational skills and understand different principles that made this project a success, as well as a special thanks to Assoc Prof Dr Prayoonsak Pluengphon, Dr Annop Ektarawong, and my research team in Extreme Conditions Physics Research Laboratory.

Secondly, I wish to thank the members of my thesis committee Assoc Prof Dr Sutee Boonchui, Asst Prof Dr Thiti Taychatanapat, Dr Rangsim Chanphana, Dr Chayanit Asawatangtrakuldee, for generously offering their time, support, guidance and good will throughout the preparation and review of this document.

Finally, I would like to thank my parents and the strong support from the Science Achievement Scholarship of Thailand (SAST).

TABLE OF CONTENTS

	Page
.....	iii
ABSTRACT (THAI).....	iii
.....	iv
ABSTRACT (ENGLISH).....	iv
ACKNOWLEDGEMENTS.....	v
TABLE OF CONTENTS.....	vi
TABLE OF FIGURES.....	1
1. Introduction.....	4
1.1. Superconductivity in Mg/Ca-substituted hexahydride.....	4
1.2. A hybrid organic-inorganic perovskite and the vdW interactions.....	5
1.3. Data-driven analyses and a substituted alloy perovskite $\text{CH}_3\text{NH}_3\text{BiSe}_2$	6
2. Theoretical Background.....	8
2.1. Many-body problems.....	8
2.2. Hartree scheme.....	8
2.3. Hartree-Fock approximation.....	9
2.4. Density functional theory.....	10
2.4.1. <i>Hohenberg-Kohn theorems</i>	10
2.4.2. <i>Self-consistent Kohn-Sham equation</i>	11
2.5. The local density approximation and Generalised gradient approximation.....	13
2.6. Techniques of calculations in DFT.....	14
2.6.1. <i>Plane waves and reciprocal space</i>	14

2.6.2. <i>Energy convergence of the plane wave basis set</i>	15
2.6.3. <i>Geometry optimisation</i>	16
2.6.4. <i>Electronic band structure</i>	16
2.6.5. <i>Density of states</i>	16
2.7. Cluster expansion	17
2.8. Phonons and electron-phonon coupling	17
2.9. BCS theory and the evaluation of superconducting critical temperature.....	18
2.10. The van de Waals interactions	22
2.11. Spin-orbit coupling	23
2.12. Artificial neural network.....	24
3. Superconducting metal hydrides $Mg_{0.5}Ca_{0.5}H_6$	26
3.1. Computational details	26
3.2. Results and discussion.....	26
3.2.1. <i>Structural stability</i>	26
3.2.2. <i>Electronic stability</i>	28
3.2.3. <i>Phonon dispersion</i>	30
3.2.4. <i>Spectral function and superconductivity critical temperature</i>	32
4. $CH_3NH_3PbI_3$ perovskite and the vdW corrections	37
4.1. Computational details	37
4.2. Results and discussion.....	37
4.2.1. <i>Energy barriers</i>	37
4.2.2. <i>Dipolar configurations under pressures</i>	40
5. $CH_3NH_3BiSe_2$ perovskite and its energy landscape	46
5.1. Computational details	46

5.2. Results and discussion.....	47
5.2.1. Multi-dimensional energy landscape.....	47
5.2.2. Neural network	50
6. Conclusions	53
Appendices.....	54
A. Energy minimisation	54
B. The generalised gradient approximation.....	55
C. Atomic positions	57
i. $Mg_{0.5}Ca_{0.5}H_6$	57
ii. $MAPbI_3$	57
iii. $MABiSeI_2$	58
REFERENCES	59
VITA	72

TABLE OF FIGURES

Figure 1 Schematic diagram for solving self-consistent Kohn-Sham equation.....	12
Figure 2 Temperature-dependent resistivity	19
Figure 3 The contour plot of T_c equation.....	22
Figure 4 A typical perceptron.	25
Figure 5 Fully connected feed-forward neural network.....	25
Figure 6 The formation energy (eV/atom) and the corresponding convex hull of the $Mg_{1-x}Ca_xH_6$ at 200 GPa. Two end points account for the binary phases of MgH_6 and CaH_6 both adopting the bcc structures, as calculated from the same computational settings for comparison. The “Known str” structures are denoted by orange pentagons. The crosses indicate structures “predicted” based on the CE technique. The ground-state “DFT GS” entities are represented by red circles.	27
Figure 7 The body-centred cubic structure of $Mg_{0.5}Ca_{0.5}H_6$. H atoms are denoted by light pink spheres, whereas orange and blue spheres account for Mg and Ca atoms, respectively. The positions of metal atoms are interchangeable due to symmetry.	28
Figure 8 The electronic band structure and pDOS of $Mg_{0.5}Ca_{0.5}H_6$ at 200 GPa.	29
Figure 9 Brillouin zone of body-centred cubic lattice [116].....	29
Figure 10 Fermi surfaces of $Mg_{0.5}Ca_{0.5}H_6$ at 200 GPa.	30
Figure 11 The calculated phonon dispersion of $Mg_{0.5}Ca_{0.5}H_6$ at 200 GPa (left); the corresponding partial phonon DOS (middle); the EPC spectral function and its cumulative EPC parameter.	30
Figure 12 The phonon density of states under pressures ranging from 200 to 400 GPa.	31
Figure 13 The EPC constant and the logarithmic frequency plotted along pressures.	32
Figure 14 T_c as a function of pressure.....	34
Figure 15 A contour plot of T_c as a function of ω_1 and ω_2	35
Figure 16 Spectral function of each pressure.....	35

- Figure 17 The cubic structure of MAPI with a lattice parameter of 6.317 Å. The MA cation consists of C (brown), N (blue), and H (pink) atoms.....38
- Figure 18 Total energy per cation profiles at different organic molecular orientations calculated by various functionals, when the lowest total energy is taken as a reference; Inset illustrates an applied anticlockwise rotation about the a-axis for the MA cation.38
- Figure 19 Different pairs of bond-lengths calculated by PBEsol and vdW-DF-cx functionals, respectively.40
- Figure 20 The relationship between enthalpy difference (eV) and pressure (GPa) calculated by vdW-DF-cx is fitted by 3rd -order Birch – Murnaghan equation of states.41
- Figure 21 Two types of voids forming in MAPI. Simplified notations of the structure and voids are introduced. S_n denotes a spherical void; x-D, y-D, and z-D indicate dumbbell voids in their respective orientation. The MA cation in S_n (a) and x-D void (b).....42
- Figure 22 Schematic orientation of the CH_3NH_3 (MA) molecules. The diagram plane is in xy-plane and the lower diagrams show the bottom layer of the cell. Light red squares are the sphere voids (denoted by $[S]_n$), and green squares denote the dumbbell-like voids (denoted by $[(x, y, z)-D]_n$, where $n = 1$ indicates voids in lower layer and $n = 2$ for the upper layer of the simulation cell. Arrows/symbols in the diagrams represent the orientation of the MA molecules inside each void. The arrow head is N and the tail C. Circle \odot means that the arrow is pointing outward from the paper and the cross \otimes means that the arrow is pointing into the paper.43
- Figure 23 Schematic orientation of MA molecules. By structural optimisation starting from Scheme C in (a), the MA evolved into (b) and (c) at low pressure (0.55–2.5 GPa), and (d) at higher pressure (2.7–3.83 GPa). Cr means relaxed SCHEME C.....43
- Figure 24 Energies of all schemes under pressures. Energy of SCHEME A is selected as a reference.....45
- Figure 25 The cubic structure of $\text{CH}_3\text{NH}_3\text{BiSeI}_2$ (MABiSeI) with labelled atoms (a); the definition of the Euler angles (b) for the MA cation where the N–C bond is directed to the N-axis. The first rotation is rotated anticlockwise through angle Φ about the c-axis (c). The second rotation is anticlockwise via angle Θ about the a'-axis or N-axis (d). Finally, the third rotation is

rotated anticlockwise through angle Ψ about the c'axis (e). Note that all atoms of the inorganic BiSeI₂ cage were kept fixed throughout the calculations, while the organic MA cation was the only thing to reorient according to the Euler's rotations. Nearly all figures are generated by VESTA [141].46

Figure 26 Energy population distribution accounting for various orientations of the MA cation, as split into 100 bins.48

Figure 27 Four – dimensional plot of $E - E_0$ (meV/atom) with respect to the Eulerian angles.....48

Figure 28 Three-dimensional and contour plots of $E - E_0$ with $\phi = 45^\circ$49

Figure 29 Energy landscape corresponding to $\psi = 0^\circ$ 50

Figure 30 Training set (80% of the total samples) and test set (the other 20%) are randomly split.51

Figure 31 Variation of the RMSE of the training set (green) and test set (red) with respect to the number of hidden layers (a), and to the number of artificial neurons for each hidden layer (b). ...51

Figure 32 Representative plots for the predictions of the optimised ANN with 80% for training and 20% for testing, with training set RMSE = 0.28 meV/atom and test set RMSE = 0.39 meV/atom.....52

CHAPTER I

Introduction

Electricity has already become indispensable part of human activities around the globe. Burning fossil fuels to get electricity to serve our insatiable desire in turn produces a ridiculous amount of greenhouse gases (34 billion tonnes in the year 2000 [1]) which consequently contributes to global warming. Another point of concern is waste heat, a largely unwanted by-product of doing work, that are ubiquitously dissipated from our electrical appliances, be they our smartphone, the fridge in our kitchen, or high-power lines on a large scale. This wasted heat results from the resistance in a material due to electrons scattering off other atoms. However, materials that circumvent this problem by allowing electricity to flow efficiently through them, without generating unwanted heat, are superconductors.

1.1. Superconductivity in Mg/Ca-substituted hexahydride

The first superconductor, mercury, was discovered by K. Onnes in 1911 [2]. Amongst the superconductors that are based on the BCS theory [3], a non-copper-oxide MgH_2 was discovered in the start of the 21st century to conventionally superconduct with $T_c = 39$ K [4], which was the highest in all its class then. Due to the synthetic processes being economical and non-toxic, MgB_2 has undoubtedly offered tremendous possibilities for applications in superconducting technology. The T_c value evaluated based on the well-known BCS (Bardeen-Cooper-Schrieffer) theory [3] was once thought to be limited by a material's electron-phonon coupling constant and maximum phonon frequency. Therefore, MgB_2 had kept its record of T_c in the class of the BCS-based superconductors for more than a decade.

Ever since the emergence of high-pressure physics, the limitations in the parameters of the BCS theory have been enhanced unprecedentedly. Very recently, significant discoveries of the BCS-based superconducting compounds under high pressures have been made, all of which involve hydrogen atoms being as a main composition. These findings include the theoretical prediction in 2014 of the superconducting H_3S compound with $T_c \sim 200$ K at 200 GPa [5] with its superconducting properties confirmed experimentally a year later [6] as well as the findings of a large number of hydrogen-rich metals, some of which superconduct under high pressures. Interestingly enough, a high $T_c \sim 280$ K at high pressure of LaH_{10} with a sodalite-like clathrate structure [7, 8] was calculated in 2017 and was subsequently confirmed by experiments two years later with a slightly deviated $T_c \sim 260$ K at 188 GPa [9]

The determining factors to achieving the near-room-temperature superconductivity in hydrogen-rich metallic compounds are associated with two essential mechanisms that involve the unique properties of hydrogen. The first one implies the contribution of hydrogen atoms to the electronic structure, especially at the Fermi energy, and the second one involves strong hydrogen vibrational effects on the electron-phonon coupling. In view of

the role played by metals, there was also a theoretical suggestion on the increase of the electron density of states at the Fermi level by metal substitution. A notable example is nothing but the Li-substitution in the MgH_{16} clathrate structure which resulted in $\text{Li}_2\text{MgH}_{16}$ with $T_c \sim 473$ K at 250 GPa [10]. This material signalled a new era of the previously proposed “hot” superconductors that have yet to be confirmed by experiment.

In this thesis, a new decoration of Mg/Ca-substituted metal hexahydride is determined by employing a metal substitution technique based on the state-of-the-art density functional theory. Starting from considering recent theoretical studies on metal hexahydrides, it has been found that MgH_6 with a sodalite-like clathrate structure becomes a conventional BCS superconductor with $T_c \sim 260$ K at 300 GPa [11] while the isostructural CaH_6 superconducts at 150 GPa with $T_c \sim 175 - 235$ K [12]. It turns out that the Ca-based hexahydride has a higher T_c values at higher pressures, whereas the Mg/Ca-based hexahydride superconducts at lower pressures [13].

1.2. A hybrid organic-inorganic perovskite and the vdW interactions

As mentioned in the first section, ever since the industrial revolution, the increasing prosperity of the world and economic growth have insatiably demanded for ever more access to affordable, clean, and reliable sources of energy due directly to the limited energy sources available on Earth. Our energy use in the 21st century must inevitably be sustainable [13]. Amongst the promising renewable energy resources, solar energy plays a predominant role due to it being the cleanest, abundant, and inexhaustible (it can stay up to 5 billion more years [14].) of all so far. And to harvest this unlimited natural resource, photovoltaic technology is one of the best ways to do that [15]. Synergism between theoretical tools and experimental advances enables many breakthroughs and has recently suggested a trend towards solid-state sensitised solar cells, amongst which perovskite solar cells assert their dominance [16].

The emergence of hybrid organic-inorganic perovskites (HOIPs) has attracted tremendous attention due particularly to their potential applications, for example, in optoelectronic and photovoltaic technology [17-21]. The interaction between the embedded molecular cations and the inorganic framework [23] observed through energy-landscape analyses [24-26] as well as the structural and dynamical nature of such systems and the presence of ferroelectric domains that reduce the rate of electron-hole pair recombination were suggested [22], to impact upon the photovoltaic performance of these materials. Regarded as the most familiar archetypal HOIPs, Methylammonium lead iodide perovskite (MAPI) and Formamidinium lead iodide (FAPbI₃) photovoltaic cells are comparatively inexpensive and also easy to assemble [27]. MAPI solar cell has recently gained the efficiency up over 22% [28-30], while by using a mixture of Cs and I/Br, the Cs/FA/Br/I-mixed HOIP was demonstrated the feasibility of achieving more than 25%-efficient tandem cells [31].

The innovative and low-cost synthetic designs of the materials mentioned earlier deliver hopeful prospect for the commercialisation of the perovskite solar cells, although there are still many challenges that have yet to be solved, e.g. reducing non-radiative recombination and increasing conductivity of device layers [32]. One major problem remains that HOIPs are extremely unstable, i.e., they are susceptible to degradation when exposed to humidity, ultraviolet light, and thermal stress [20, 33-35]. The average lifespan of the most

investigated perovskite solar cells is found to be in the order of weeks to only several months [36]. Even the most stable cell reported was confirmed to last only for over a year under controlled conditions [37], still unfledged in a world dominated by the well-established silicon solar cells. Regarding theoretical investigations, especially based on the density functional theory (DFT), the stability issues have reportedly been addressed in the context of dispersive interaction, for instance, it was acknowledged that the van der Waals (vdW) interaction between the PbI_6 octahedra and the methylammonium (MA) cation plays a significant role in electronic property, as investigated by dispersion-corrected DFT [38], as well as the computational predictions of structural parameters that substantiate the vdW interactions among the halide atoms and hydrogen bonding [39, 40].

Interestingly, crystal structures can straightforwardly be morphed without any chemical modification, whose changes in atomistic geometry and bonding characteristics are achieved, by pressurisation, which was observed in methylammonium lead halide perovskites [49-51]. When pressurised, the synthesised MAPI was demonstrated to undergo a series of structural phase transitions [50, 52]. Under ambient conditions, the material adopts a tetragonal phase II (space group of $I4/mcm$) structure in the temperature ranging from 165 K to 321 K [23] and the pressure up to 0.35 GPa, while it morphs into a cubic phase IV ($Im\bar{3}^-$), structure at pressures 0.3–2.5 GPa and isostructural cubic phase V ($Im\bar{3}^-$) above 2.5 GPa [52]. Also, experimental data corroborates the physical distinction between phases IV and V in terms of molecular volumes, Pb–I bond lengths, Pb–I–Pb bond angles, and the energy band gaps, which in principle exhibit disruptive jumps during structural phase transitions [23].

To this end, the effects of the organic molecular orientations on structural property of phases IV and V are investigated in relation to the available experimental results [53] by employing the first-principles calculations based on DFT with the vdW corrections. The rigid flips of the MA cation are applied to determine the total energy profiles that account for varying types of dispersion-corrected versions of exchange-correlation functionals, which are proposed to significantly affect our models. It is found that vdW interactions influence the energy barriers of the MA cation embedded in the inorganic framework of PbI_6 when calculated by different types of functionals. Also, the series of cationic orientational configurations in a supercell suggest a relatively stable structure for MAPI under pressures.

1.3. Data-driven analyses and a substituted alloy perovskite $\text{CH}_3\text{NH}_3\text{BiSeI}_2$

As mentioned earlier, HOIPs have become the centre of attention in photovoltaic research due to their highly potential applications. The fundamental structural and dynamics of the $\text{HC}(\text{NH}_2)_2$ (FA) cation in FAPbI_3 perovskite have been investigated by the aid of the Eulerian angles. The results imply the preferable orientations for the organic molecules in a unit cell, which lead eventually to the Rashba effect or electronic band splitting [24] as well as the full energy landscape for the rigid flips and translations of CH_3NH_3^+ in the MAPbI_3 perovskite [22]. One key factor, however, that facilitates the high efficiency of halide perovskites is the use of lead (Pb) which is toxic [54].

The structural and electronic properties of environmentally-friendly $\text{CH}_3\text{NH}_3\text{BiSiI}_2$ and $\text{CH}_3\text{NH}_3\text{BiSeI}_2$ perovskites were predicted [63] by means of the anion-splitting approach, that is, replacing one I atom with Se atom and Pb atom with Bi atom to satisfy the charge

neutrality, to yield optimal band gaps for solar absorbers in accordance with the Shockley–Queisser detailed balance limit of efficiency [44].

Therefore, $\text{CH}_3\text{NH}_3\text{BiSe}_2$ perovskite, or MABiSeI hereafter, is regarded as a promising candidate for photovoltaic materials, and is studied to gain some insight into such an eco-friendly solar cell. Never before has the interplay between the organic CH_3NH_3 (MA) molecule and the inorganic octahedral framework of BiSe_2 been studied by means of total energy analyses. Thus, the organic–inorganic linkage was thoroughly probed by an effective, systematic method called the Euler's rotations applied to the MA cation. The Eulerian angles occupy the cubo-octahedral cavity between the corner-sharing octahedra of BiSe_2 , thereby resulting in the beyond-three-dimensional energy landscape. The high-dimensional energy landscape was obtained from the total energies of the cubic MABiSeI, which were evaluated based on DFT [64], subtracted by the relatively lowest one in all of the samples. And also due to the massive amount of generated data obtained from DFT, a reliable model is required to recognise the underlying relationships in the dataset, e.g., the total energies and the Eulerian angles. Being the quintessential deep learning models, deep artificial neural networks offer the capability to create accurate models quickly and automatically [65]. In this work, we use a deep neural network to develop a predictive model for the energy determinations of MABiSeI at various Eulerian-rotated orientations of the MA cation. This approach encourages a paradigm shift in the energy calculations for this class of materials without fully employing computationally demanding DFT calculations.

CHAPTER II

Theoretical Background

In this chapter, all theoretical framework employed extensively in this thesis are discussed.

2.1. Many-body problems

Ever since the advent of quantum mechanics, one of the crucial goals of physics has always been the description of many-particle systems. Solving for analytic solutions for the Schrodinger equation are practicable for just a few simple systems yet still a tall order for other complicated solid-state systems. If one is to investigate properties of an interacting system consisting of n electrons and N nuclei with charges Z_I , the many-body Schrodinger Hamiltonian (SE) in Hartree atomic units is written as,

$$H = -\frac{1}{2} \sum_{i=1}^n \nabla_i^2 - \frac{1}{2} \sum_{I=1}^N \frac{1}{M_I} \nabla_I^2 + \frac{1}{2} \sum_{i \neq j}^n \frac{1}{|\vec{r}_i - \vec{r}_j|} - \sum_{i=1}^n \sum_{I=1}^N \frac{Z_I}{|\vec{r}_i - \vec{R}_I|} + \frac{1}{2} \sum_{I \neq J}^N \frac{Z_I Z_J}{|\vec{R}_I - \vec{R}_J|}. \quad (1)$$

The small and capital letters respectively denote electron and nuclei. The first two terms on the right-hand side of equation(1) are the kinetic energy of electrons and nuclei, respectively, where the nuclear mass at site I is represented as M_I . Due to electrically charged particles, the following three terms are Coulombic interactions arising from electron-electron, electron-nucleus, and nucleus-nucleus. The vector \vec{r}_i indicates the electron's position at site i , while \vec{R}_I refers to nuclear position at site I .

Now if the effect from nuclei in the electronic problem are omitted due to the fact that the nuclei are much heavier than the electrons (an electron itself is approximately 2000 times lighter than a proton), thereby moving relatively more slowly, this scheme is the so-called Born-Oppenheimer approximation [66]. To put it another way, the ions (nuclei) are essentially stationary as seen from the electrons. As a consequence, the kinetic and the nucleus-nucleus interaction terms become constants, and that the Hamiltonian is now expressed as,

$$H = -\frac{1}{2} \sum_{i=1}^n \nabla_i^2 + \frac{1}{2} \sum_{i \neq j}^n \frac{1}{|\vec{r}_i - \vec{r}_j|} - \sum_{i=1}^n \sum_{I=1}^N \frac{Z_I}{|\vec{r}_i - \vec{R}_I|}. \quad (2)$$

Now it is not uncommon to consider the many-electron wave function, $\Psi(\vec{r}_1, \vec{r}_2, \dots, \vec{r}_N)$, where the particle coordinates and spins are denoted as \vec{r}_i .

2.2. Hartree scheme

It was Hartree [67] who introduced the approximate many-electron wave function as a product of single-particle functions, that is,

$$\bar{\Psi}(\bar{r}_1, \bar{r}_2, \dots, \bar{r}_N) = \psi_1(\bar{r}_1) \psi_2(\bar{r}_2) \cdots \psi_N(\bar{r}_N). \quad (3)$$

The many-body problem now is reduced to an uncoupled problem in which each of the functions $\psi_i(\bar{r}_i)$ satisfies a one-electron SE, and that the interaction of one electron with the remaining ones is incorporated in an averaged way into a potential felt by the electron, i.e.,

$$\left[-\frac{1}{2} \nabla^2 + V_{ext} + \Phi_i \right] \psi_i(\bar{r}) = \varepsilon_i \psi_i(\bar{r}), \quad (4)$$

where the Coulomb potential Φ_i (also known as the Hartree potential) is defined by Poisson's equation

$$\nabla^2 \Phi_i = \sum_{j \neq i}^n |\psi_j|^2, \quad (5)$$

and V_{ext} describes the interaction due to the nuclei. The SE for the Hartree scheme can be written as

$$\left[-\frac{1}{2} \nabla^2 - \sum_{i,I} \frac{Z_I}{|\bar{r}_i - \bar{R}_I|} + \sum_{j \neq i} \int d\bar{r}' |\psi_j(\bar{r}')|^2 \frac{1}{|\bar{r} - \bar{r}'|} \right] \psi_i(\bar{r}) = \varepsilon_i \psi_i(\bar{r}). \quad (6)$$

The Hartree potential (the integral term) is the potential resulting from a charge distribution caused by all other the electrons but the i^{th} electron itself. Essentially, one can discuss the properties of an interacting system by solving for equation(6) self-consistently.

2.3. Hartree-Fock approximation

In the previously section, the many-electron wave function can be approximated as a product of single-particle functions, which is, obviously, incorrect. This model fails to describe the true nature of electronic properties since it violates the anti-symmetry of the wave function. To improve the circumstance, Hartree and Fock, hence Hartree-Fock theory [68], proposed that the many-electron wave function must be defined as a determinant of many single-electron wave functions, as also called the "Slater determinant", that explicitly includes the anti-symmetric properties of the electrons:

$$\Psi_{AS}(\bar{x}_1, \bar{x}_2, \dots, \bar{x}_N) = \frac{1}{\sqrt{N!}} \begin{vmatrix} \psi_1(\bar{x}_1) & \psi_2(\bar{x}_1) & \cdots & \psi_N(\bar{x}_1) \\ \psi_1(\bar{x}_2) & \psi_2(\bar{x}_2) & \cdots & \psi_N(\bar{x}_2) \\ \vdots & \vdots & \ddots & \vdots \\ \psi_1(\bar{x}_N) & \psi_2(\bar{x}_N) & \cdots & \psi_N(\bar{x}_N) \end{vmatrix}. \quad (7)$$

Therefore, one can now evaluate the total energy of an interacting system according the HF approximation by solving

$$\begin{aligned}
F\psi_i(\vec{r}) &= \varepsilon_i\psi_i(\vec{r}) \\
&= \left[-\frac{1}{2}\nabla^2 - \sum_{i,I} \frac{Z_I}{|\vec{r}_i - \vec{R}_I|} \right] \psi_i(\vec{r}) + \sum_{j \neq i} \int d\vec{r}' |\psi_j(\vec{r}')|^2 \frac{1}{|\vec{r} - \vec{r}'|} \psi_i(\vec{r}) \\
&\quad - \sum_j \delta_{\sigma_i \sigma_j} \int d\vec{r}' \frac{\psi_j^*(\vec{r}')\psi_i(\vec{r}')}{|\vec{r} - \vec{r}'|} \psi_j(\vec{r}),
\end{aligned} \tag{8}$$

where F is the Fock operator and the first three terms on the right-hand side of equation(8) are the same as in those appearing in equation(6). The last term corresponds to the exchange term, which implies that electrons of like-spin avoid each other. Every electron is now surrounded by an “exchange hole” in which other electrons having the same spin are hardly found.

This approach is regarded as an indispensable benchmark in molecular physics, yet still complicated systems such as solids continue to be problematic, i.e., systems containing a large number of electrons require expensive computation costs and huge memory resources. Infamously, HF scheme underestimates cohesive energies in many metals, e.g. it yields positive cohesive energy of Li [69], which is unbelievably absurd.

2.4. Density functional theory

Fortunately, enough, one can tackle interacting many-particle problems by making use of a decent, promising tool called the density functional theory.

2.4.1. Hohenberg-Kohn theorems

Proposed in 1964 by Hohenberg and Kohn [64], the density functional theory (DFT) is regarded as one of the most reliable, successful, and seemingly most adopted approaches to investigating ground-state energies and electronic structures of interacting many-body quantum systems. The Hohenberg – Kohn theorems state that:

- for any system of interacting particles with an external potential $V_{ext}(\vec{r})$, there exists a one-to-one correspondence between the external potential and the system’s ground-state density $\rho(\vec{r})$. Moreover, the ground-state expectation value of any observable quantity A is a unique function, that is:

$$\langle \Psi | \hat{A} | \Psi \rangle = A[\rho_0(\vec{r})]. \tag{9}$$

- Also, for an arbitrary external potential applied to an interacting system, it is possible, in principle, to exactly define a universal total energy functional of density, which is expressed as

$$E[\rho(\vec{r})] = E_{HK}[\rho(\vec{r})] + \int V_{ext}(\vec{r})\rho(\vec{r})d\vec{r}. \tag{10}$$

The term E_{HK} is regarded as the universal constant not explicitly relating to any information of any types of nuclei or their spatial positions. Despite unknown, this arbitrarily universal constant determines the GS energy of a system by minimising

total energy with respect to density by means of the variational principle, which can be written as (the full derivation can be seen in Appendix A),

$$\delta E[\rho(\vec{r})] \Big|_{\rho=\rho_0} = 0. \quad (11)$$

The exact GS energy E_0 accounting for the GS density $\rho_0(\vec{r})$ is defined to be

$$E_0 = E[\rho_0(\vec{r})] \leq E[\rho(\vec{r})]. \quad (12)$$

2.4.2. Self-consistent Kohn-Sham equation

As a result of the previous section, the density parameter can be employed as the main quantity used to calculate all observables. According to Kohn and Sham [70], the challenge of finding good approximations to the energy functional is considerably simplified by using

$$E[\rho] = T_0[\rho] + \int d\vec{r} \rho(\vec{r}) \left[V_{ext}(\vec{r}) + \frac{1}{2} \Phi(\vec{r}) \right] + E_{xc}[\rho]; \quad (13)$$

the non-interacting kinetic energy of a system with density ρ is denoted by T_0 , Φ is the classical Coulomb potential for electrons, and the E_{xc} is regarded as the exchange-correlation energy. The external potential $V_{ext}(\vec{r})$ results from nuclei and the inner shells' electrons. Clearly, one can use the electron density $\rho(\vec{r})$ as a basic variable instead of laboriously solving for the many-electron Hamiltonian in equation(2). The Schrodinger-like Kohn-Sham equation for non-interacting particles thus becomes

$$\left[-\frac{1}{2} \nabla^2 - \sum_{i,I} \frac{Z_I}{|\vec{r}_i - \vec{R}_I|} + \int d^3\vec{r}' \rho(\vec{r}') \frac{1}{|\vec{r} - \vec{r}'|} + V_{xc}[\rho](\vec{r}) \right] \psi_i^{KS}(\vec{r}) = \varepsilon_i \psi_i^{KS}(\vec{r}), \quad (14)$$

which yields

$$\rho(\vec{r}) = \sum_{i=1}^n |\psi_i^{KS}(\vec{r})|^2. \quad (15)$$

The noticeable difference between the HF and KS schemes is that the Hamiltonian of the former depends upon the individual orbitals, whereas that of the latter is a functional of electron density. Now the GS energy can be evaluated by minimising $E[\rho(\vec{r})]$ with respect to the density according to equations(11) and (12). One can achieve energy minimisation by means of the Euler's equation with a Lagrange multiplier. The KS orbital in atomic unit can now be written as

$$\left[-\frac{1}{2} \nabla_i^2 + V_{eff}(\vec{r}) \right] \psi_i^{KS}(\vec{r}) = \varepsilon_i \psi_i^{KS}(\vec{r}), \quad (16)$$

where the effective potential is defined as

$$V_{eff}(\vec{r}) = V_{ext}(\vec{r}) + V_H[\rho(\vec{r})] + V_{xc}[\rho(\vec{r})], \quad (17)$$

with the Hartree potential,

$$V_H[\rho(\vec{r})] = \int \frac{\rho(\vec{r}')}{|\vec{r} - \vec{r}'|} d\vec{r}', \quad (18)$$

and the exchange-correlation potential,

$$V_{xc}[\rho(\vec{r})] = \frac{\delta}{\delta\rho(\vec{r})} E_{xc}[\rho(\vec{r})]. \quad (19)$$

The KS equation enables one to investigate any complex quantum systems by effectively mapping an interacting system into a fictitious non-interacting system in which the particle is moving.

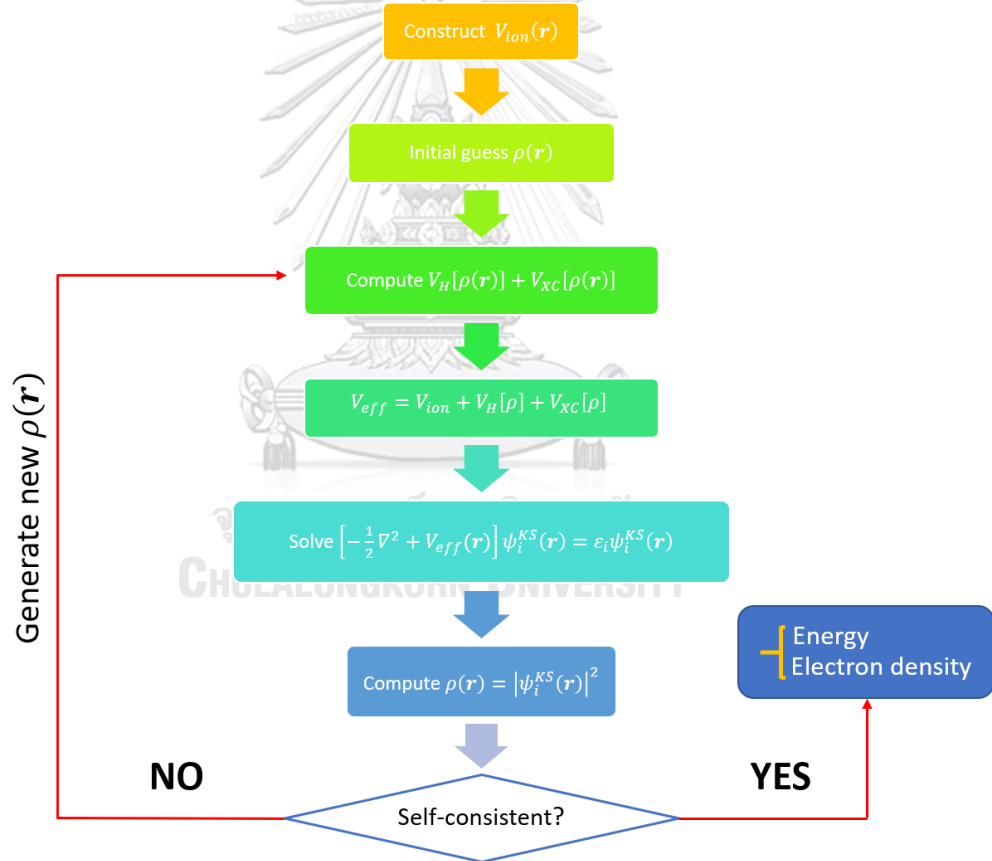


Figure 1 Schematic diagram for solving self-consistently the Kohn-Sham equation.

As illustrate in Figure 1, the KS equation is solved iteratively. First of all, the initial density is randomised in order to determine the effective potential, then the equation is solved for the total energy and the KS orbital, which are then used in the subsequent step. The self-consistent process runs until it is stopped due to fulfilment of the convergence criterion. In

equation(17) all the terms but the exchange-correlation potential $V_{xc}[\rho(\vec{r})]$ can be evaluated exactly, and that the approximations for E_{xc} is unavoidable.

2.5. The local density approximation and Generalised gradient approximation

By far the simplest, oldest, and supposedly the most important model of E_{xc} is the local density approximation (LDA), which was proposed in their original paper by Hohenberg and Kohn [64]. In LDA scheme, the exchange-correlation energy is associated with a homogeneous electron gas of the same density. The LDA is solely dependent upon the local density, and the total energy can be expressed as,

$$E_{xc}^{LDA}[\rho(\vec{r})] = \int d\vec{r} \rho(\vec{r}) \varepsilon_{xc}^{\text{hom}}[\rho(\vec{r})]. \quad (20)$$

The term ε_{xc} can be decomposed into exchange and correlation energies per particle,

$$\varepsilon_{xc}[\rho] = \varepsilon_x[\rho] + \varepsilon_c[\rho], \quad (21)$$

where the exchange energy of a homogeneous electron (Thomas-Fermi-Dirac model [71]) gas at density ρ is

$$E_x^{\text{hom}}[\rho(\vec{r})] = -\frac{3}{4} \left(\frac{3}{\pi} \right)^{1/3} \int \rho^{4/3}(\vec{r}) d\vec{r}, \quad (22)$$

whereas $E_c[\rho(\vec{r})]$ is evaluated from an interpolation formula [72] that links between the known limiting form of $\varepsilon_{xc}^{\text{hom}}[\rho(\vec{r})]$ in the high [73, 74] and low [75] density regimes.

$$\varepsilon_x^{\text{hom}}[\rho(\vec{r})] = -\frac{3}{4} \left(\frac{3}{\pi} \right)^{1/3} \rho^{1/3}(\vec{r}) \quad (23)$$

A model developed by Perdew and Zunger [76] is commonly used as the correlation formula that exploits data, as calculated by the quantum Monte Carlo method, of the homogeneous electron gas reported by Ceperly et al [77]. Despite its simplicity, although LDA succeeds in solid-state systems, it notoriously tends to overbind and fails to describe molecules.

Alternatively, the model was then modified to describe more complex systems as an extension of LDA, which is known as the generalised gradient approximation (GGA). The GGA is currently regarded as the most popular exchange-correlation functional in condensed matter physics. Not only is the electron density, $\rho(\vec{r})$, included in the exchange-correlation term, but its gradient, $\nabla\rho(\vec{r})$, is also incorporated (see Appendix B for more detail), which can be expressed as,

$$E_{xc}^{GGA}[\rho(\vec{r})] = \int d\vec{r} \rho(\vec{r}) \varepsilon_{xc}[\rho(\vec{r}), \nabla\rho(\vec{r})]. \quad (24)$$

2.6. Techniques of calculations in DFT

2.6.1. Plane waves and reciprocal space

If one considers a continuous periodic solid, invariant under translational and rotational symmetries, any orbital can be defined as,

$$\phi_{i\bar{k}}(\vec{r}) = \frac{1}{\sqrt{\Omega}} \sum_{\vec{G}} c_{i\bar{k}}(\vec{G}) e^{i(\bar{k}+\vec{G})\cdot\vec{r}} = FT^{-1} [c_{i\bar{k}}(\vec{G})], \quad (25)$$

where the reciprocal space representation of the orbital is constituted by a set of complex coefficients $c_{i\bar{k}}(\vec{G})$, with \vec{G} being the reciprocal lattice vectors. Equation(25) is constrained to relations,

$$\begin{aligned} \int d\vec{r} \phi_{i\bar{k}}^*(\vec{r}) \phi_{i\bar{k}}(\vec{r}) &= 1, \\ \sum_{\vec{G}} c_{i\bar{k}}^*(\vec{G}) c_{i\bar{k}}(\vec{G}) &= 1. \end{aligned} \quad (26)$$

By means of Fourier transform, thus,

$$c_{i\bar{k}}(\vec{G}) = FT[\phi_{i\bar{k}}(\vec{r})] = \frac{1}{\sqrt{\Omega}} \int d\vec{r} \phi_{i\bar{k}}(\vec{r}) e^{-i(\bar{k}+\vec{G})\cdot\vec{r}}. \quad (27)$$

It is also useful to represent other quantities, e.g. densities, in this way. The reciprocal representation of the density $\rho(\vec{G})$ can be written as,

$$\begin{aligned} \rho(\vec{r}) &= \frac{1}{\Omega} \sum_{\vec{G}} \rho(\vec{G}) e^{i\vec{G}\cdot\vec{r}}, \\ \rho(\vec{G}) &= \int d\vec{r} \rho(\vec{r}) e^{-i\vec{G}\cdot\vec{r}}. \end{aligned} \quad (28)$$

It becomes much easier to evaluate the non-interacting kinetic energy T_s , the Hartree energy E_H as well as its potential. Now if we consider

$$\begin{aligned} -\frac{1}{2} \nabla^2 \phi_{i\bar{k}}(\vec{r}) &= -\frac{1}{2} \nabla^2 \left(\frac{1}{\sqrt{\Omega}} \sum_{\vec{G}} c_{i\bar{k}}(\vec{G}) e^{i(\bar{k}+\vec{G})\cdot\vec{r}} \right) \\ &= \frac{1}{2\sqrt{\Omega}} \sum_{\vec{G}} c_{i\bar{k}}(\vec{G}) (\bar{k} + \vec{G})^2 e^{i(\bar{k}+\vec{G})\cdot\vec{r}}. \end{aligned} \quad (29)$$

Now the non-interacting kinetic energy T_s becomes,

$$\begin{aligned} T_s &= \left\langle \phi_{i\bar{k}}(\vec{r}) \left| -\frac{1}{2} \nabla^2 \right| \phi_{i\bar{k}}(\vec{r}) \right\rangle \\ &= \frac{1}{2} \sum_{i\bar{k}} \sum_{\vec{G}} c_{i\bar{k}}^*(\vec{G}) c_{i\bar{k}}(\vec{G}) (\bar{k} + \vec{G})^2. \end{aligned} \quad (30)$$

The Hartree potential is also defined by Poisson's equation:

$$-\nabla^2 \mu_H(\vec{r}) = \rho(\vec{r}) - \langle \rho \rangle. \quad (31)$$

The reciprocal space representations of the Hartree potential and the density become

$$-\nabla^2 \left(\frac{1}{\Omega} \sum_{\vec{G} \neq 0} \mu_H(\vec{G}) e^{i\vec{G} \cdot \vec{r}} \right) = \frac{1}{\Omega} \sum_{\vec{G} \neq 0} \rho(\vec{G}) e^{i\vec{G} \cdot \vec{r}}, \quad (32)$$

with $\vec{G} \neq 0$ accounting for the subtraction of the average density in equation(31). Applying ∇^2 to the left-hand side of equation(32) and equate the exponential coefficients, so that the Hartree potential is written as,

$$\mu_H(\vec{G}) = \frac{\rho(\vec{G})}{\vec{G}^2}. \quad (33)$$

It is worth noting that the Hartree potential with $\vec{G} = 0$ exactly cancels the equivalent term from the positive nuclear charge in the neutral system.

The Hartree energy is then expressed as,

$$\begin{aligned} E_H &= \frac{1}{2} \int d\vec{r} \mu_H(\vec{r}) \rho(\vec{r}) = \frac{1}{2} \int d\vec{r} \mu_H^*(\vec{r}) \rho(\vec{r}) \\ &= \frac{1}{2} \int d\vec{r} \left(\frac{1}{\Omega} \sum_{\vec{G} \neq 0} \mu_H^*(\vec{G}) e^{-i\vec{G} \cdot \vec{r}} \right) \left(\frac{1}{\Omega} \sum_{\vec{G}' \neq 0} \rho(\vec{G}') e^{i\vec{G}' \cdot \vec{r}} \right) \\ &= \frac{1}{2\Omega^2} \sum_{\vec{G}, \vec{G}'} \mu_H^*(\vec{G}) \rho(\vec{G}') \int d\vec{r} e^{i(\vec{G}' - \vec{G}) \cdot \vec{r}} \\ &= \frac{1}{2\Omega} \sum_{\vec{G}} \mu_H^*(\vec{G}) \rho(\vec{G}). \end{aligned} \quad (34)$$

The last step in equation(34) is completed by making use of the Dirac delta function. Finally, together with equation(33), equation(34) thus becomes,

$$E_H = \frac{1}{2\Omega} \sum_{\vec{G}} \frac{\rho^*(\vec{G}) \rho(\vec{G})}{\vec{G}^2}. \quad (35)$$

2.6.2. Energy convergence of the plane wave basis set

In principle, the complete set of reciprocal vectors \vec{G} is expanded to infinite, meaning evaluating a summation overall such vectors would take eternity to complete. In practice, however, one can truncate the plane wave components that become negligible for large \vec{G} vectors. Those vectors with magnitudes larger than some cut-off radius G_{cut} will be excluded. Thus, the kinetic cut-off energy is defined as,

$$E_{cut} \leq \frac{1}{2} |G_{cut}^2|. \quad (36)$$

There is no set-in-stone rule for the appropriate value of E_{cut} in advance, as it depends upon the system in question. However, the general rule of thumb is that one increases it until stops varying. This procedure is known as a “convergence test”.

2.6.3. Geometry optimisation

The geometry optimisation is the process of searching for the configuration of atomic positions that are of minimum energies [78]. The structure in question is relaxed until the net interatomic force on each atom is satisfactorily close to zero. GO represents the structural geometry the system is expected to adopt at zero temperature. In order to avoid the difficulties in calculating finite differences ($\sim 3N$ calculations of the total energy), one can use the Hellman-Feynman Theorem [79, 80] which states,

$$\frac{dE_\lambda}{dx} = \left\langle \psi_\lambda \left| \frac{d\hat{H}_\lambda}{dx} \right| \psi_\lambda \right\rangle, \quad (37)$$

where \hat{H}_λ is a Hamiltonian operator depending on a continuous parameter λ . Equation(37) essentially implies that the derivative of the electronic energy with respect to some continuous parameter λ , such as an atomic position, is equivalent to the corresponding partially derivative in which the wave function ψ_λ , implicitly depending upon λ , is held constant. Thus, the forces on the atoms can be calculated without the need to recalculate the electronic structure. The atoms are moved in a downhill manner closer to the local energy minimum with the forces known. This process's iterations will bring about the system reaching a geometry at which the forces approaching zero, and the energy is minimised.

2.6.4. Electronic band structure

Recall that the ground-state wave function, $\psi_{i\vec{k}}(\vec{r})$, of a system can be solved from the solution to the Kohn-Sham equation, equation(16). The Kohn-Sham potential is then calculated from the GS density, and successively the corresponding eigenstates and eigenvalues that include conduction bands are obtained for the set of band structure k – points, as given by

$$\left\langle \psi_{i\vec{k}'}(\vec{r}) \left| \hat{H} \right| \psi_{i\vec{k}}(\vec{r}) \right\rangle = \varepsilon_{i\vec{k}} \delta_{\vec{k}\vec{k}'}. \quad (38)$$

2.6.5. Density of states

The electronic density of states (DOS) is conceptualised as the number of states available at each level of energy. It is interpreted mathematically as a distribution in terms of probability density function. The DOS for a given n^{th} energy level, $g(\varepsilon)$, is defined by,

$$g_n(\varepsilon) = \int \frac{d\vec{k}}{4\pi^3} \delta(\varepsilon - \varepsilon_n(\vec{k})), \quad (39)$$

where the integration is taken all over any primitive cell, and the energy eigenvalue for the n^{th} energy level is indicated by $\varepsilon_n(\vec{k})$. Likewise, the partial density of states (pDOS) corresponds to the projection of any particular orbital of the particular atom on the DOS.

2.7. Cluster expansion

Amongst numerous methodologies that enable the calculation of thermodynamic properties from DFT, the “cluster expansion (CE)” allows one to circumvent the intractability of calculating energies of various atomic arrangements. Based on the knowledge of the energies accounting for a sufficiently small number of configurations, the CE is capable of predicting the energy of any atomic configuration.

Being a method similar to the treatment of Ising model, CE is formally defined by assigning occupation variables σ_i , taking value -1 or +1, to each site i of the parental lattice. A particular configuration σ contains the value of occupation variable for each site of the parental lattice. Essentially, the CE parametrises the energy per atom of the alloy as a polynomial in the occupation variables [81]:

$$E(\sigma) = \sum_{\alpha} m_{\alpha} J_{\alpha} \left\langle \prod_{i \in \alpha'} \sigma_i \right\rangle, \quad (40)$$

where α is a cluster, a set of i , that are inequivalent symmetrically, with the average symbol taken over all clusters α' that are symmetrically equivalent to α with multiplicity m_{α} . The effective cluster interaction (ECI), denoted by J_{α} , includes the information associated with the energetics of the alloy, and can be determined by the approach known as the Structure Inversion Method (SIM) or the Collony-Williams method [82], which are evaluated by fitting the energies of a relatively small number of configurations obtained directly from DFT calculations. This method’s ability to determine the predicted structures proves useful for predicting variations of alloy structures, as the process is achieved without relying on DFT calculations except the energies accounting for some known structures, thereby making this a time-saving technique.

2.8. Phonons and electron-phonon coupling

Having been discussed so far, the DFT calculations reveal the properties of a material in which the atoms are assumed localised at equilibrium or minimum energy position. In other words, the calculations are a zero-temperature approach. However, in the real world the materials are excited with finite temperatures, i.e. the atoms in the material will vibrate about their equilibrium positions provided that the material is raised to a non-zero temperature.

Given a set of N atoms, the corresponding Cartesian coordinates are written as a vector with $3N$ components, $\vec{r} = (r_1, r_2, \dots, r_{3N})$. If \vec{r}_0 denotes atomic positions at local energy minimum of the atoms, then is not uncommon to define coordinates $\vec{x} = \vec{r} - \vec{r}_0$. The Taylor expansion to the second order of the atom’s energy about the minimum at \vec{r}_0 becomes,

$$E = E_0 + \frac{1}{2} \sum_{i=1}^{3N} \sum_{j=1}^{3N} \left(\frac{\partial^2 E}{\partial x_i \partial x_j} \right)_{\vec{x}=0} x_i x_j, \quad (41)$$

with the first derivatives (slopes) being zero as they are evaluated at the energy minimum. Now, the Hessian matrix is defined as,

$$H_{ij} = \left(\frac{\partial^2 E}{\partial x_i \partial x_j} \right)_{\bar{x}=0}. \quad (42)$$

The equation of motion for the atoms associated with the i^{th} coordinate can be written as

$$F_i = m_i \frac{d^2 x_i}{dt^2} = -\frac{\partial E}{\partial x_i}. \text{ Thus, the equation of motion in matrix form now becomes,}$$

$$\frac{d^2 \bar{x}}{dt^2} = -A\bar{x}, \quad (43)$$

with the mass-weighted Hessian matrix of which its elements are $A_{ij} = H_{ij}/m_i$. The eigenvectors and their eigenvalues of the mass-weighted Hessian matrix A are the vectors $\bar{e}_1, \bar{e}_2, \dots, \bar{e}_{3N}$ satisfying $A\bar{e} = \lambda\bar{e}$. Therefore, the general solution of equation(43) is a linear combination of the normal modes:

$$\bar{x}(t) = \sum_{i=1}^{3N} [a_i \cos(\omega t) + b_i \sin(\omega t)] \bar{e}_i, \quad (44)$$

with the frequency $\omega = \sqrt{\lambda}$. Now the main task is to calculate the elements of the Hessian matrix to determine the set of normal modes in DFT. Using finite-difference approximations, the Hessian matrix becomes,

$$H_{ij} = \left(\frac{\partial^2 E}{\partial x_i \partial x_j} \right)_{\bar{x}=0} \cong \frac{E(\delta x_i, \delta x_j) - 2E_0 + E(-\delta x_i, -\delta x_j)}{\delta x_i \delta x_j}. \quad (45)$$

2.9. BCS theory and the evaluation of superconducting critical temperature

The first discovery of superconductivity dates back to 1911 when Kamerlingh Onnes [83] cooled down mercury by liquid helium and found the resistance of mercury had decreased gradually, as expected for any particular conductors, until it suddenly plummeted to zero at 4.2 K, instead of continually approaching a value at absolute zero.

Electrical resistance is defined as an obstruction to the flow of electrons or electrical current caused by the vibrational motion of crystal lattice. When the temperature of the conducting material is elevated, the atoms start vibrating more rigorously thereby obstructing the flow of electrons. When a conductor is cooled down, on the other hand, atoms vibrate with less intensity and therefore have lower resistivity to current. At lower temperature the resistivity of a normal metal is described by $\rho(T) \propto T^5$ [84], as illustrated in Figure 2 (orange).

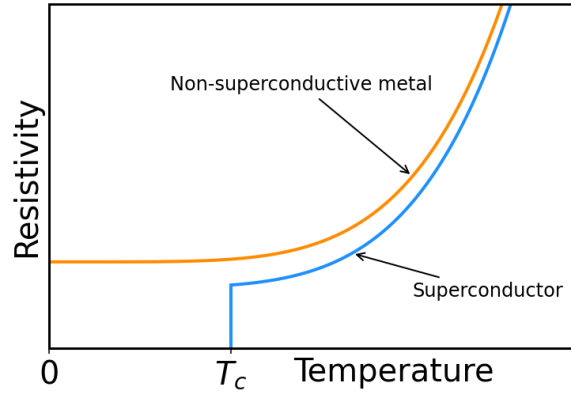


Figure 2 Temperature-dependent resistivity

However, the temperature-dependence of the resistivity/resistance remains up to a specific value, after which all resistance of the metal suddenly disappears and the transition to the superconducting state occurs (blue line in Figure 2). The temperature at which a regular conductor abruptly transitions to a superconducting state is known as the critical temperature (T_c).

The world had to wait for quite some time for someone/some ones to unravel the mysteries of superconductors. In 1957, physicists J. Bardeen, L. Cooper, and J. R. Schrieffer came up with the first microscopic, yet phenomenological theory to explain the genesis of superconductivity, hence the BCS theory [3]. The theory states that superconductivity is a consequence of the formation and condensation of multiple pairs of electrons, known as the Cooper pairs. Electrons may repel fellow ones, yet they happen to exert an attractive force on the positive ions that form the crystal lattice (arrangement of atoms, ions, or molecules). Crystal vibrations (locally excessive positive ions) mediate the creation of pairs, thereby resulting in superconductivity.

By solving for the pairing Hamiltonian on the basis of mean-field approach and variational method, the pair binding energy is expressed according to weak interaction by,

$$\Delta \approx 2\hbar\omega_c \exp\left(-\frac{1}{N_F V_{eff}}\right), \quad (46)$$

where N_F is the electron density of states at the Fermi level (ε_F), and V_{eff} denotes the effective potential arising from electron-phonon interaction, which happens to be an intractable problem in practice. Subsequently, the critical temperature for weak coupling is proposed to be,

$$T_c \approx 1.13\Theta_D \exp\left(-\frac{1}{N_F V_{eff}}\right), \quad (47)$$

with the Debye temperature Θ_D being the maximum frequency with which the ions can vibrate. Now, provided that the exponential term in equation(47) is kept constant, the critical temperature is thus inversely proportional to the square-root of mass, as given by,

$$T_c \propto \Theta_D = \frac{\hbar\omega_D}{k_B} = \frac{\hbar}{k_B} \sqrt{\frac{C}{M}}. \quad (48)$$

Note that the ions, in this case, are seen as homogeneous harmonic oscillators of mass M . The inverse relationship in equation(48) is in agreement with the Isotope effect, as previously observed experimentally [85].

As mentioned earlier, the effective potential associated with electron-coupling interacting becomes impracticable especially when the material in question is a complicated, therefore, an alternative formalism is required. In 1968, McMillan [86] proposed an approximation of T_c by solving the electronic normal and pairing self-energies [87], which essentially describes the potential felt by an electron due to the interactions of the surrounding medium with it, by means of a trial function that is a constant and disrupted at the maximum phonon frequency. As a result, a new parameter called “electron-phonon coupling constant” is introduced, and is written as,

$$\lambda \equiv 2 \int_0^{\omega_0} \alpha^2(\omega) F(\omega) \frac{d\omega}{\omega}, \quad (49)$$

where ω is the phonon frequency. The term $\alpha^2 F$, also called the “spectral function”, is related to the electron-phonon Hamiltonian explicitly depending upon the electronic matrix of the change in the crystal potential V_{crys} as one atom is moved, as can be evaluated from

$$\begin{aligned} \alpha^2 F &\propto N_F \left| \langle \vec{k}' + \vec{q} | H_{e-ph} | \vec{k} \rangle \right|^2 \\ &\propto N_F \left| \langle \vec{k}' + \vec{q} | \vec{u}_i \cdot \nabla V_{crys}(\vec{r}_i - \vec{R}_i^0) | \vec{k} \rangle \right|^2, \end{aligned} \quad (50)$$

where \vec{u} is the nuclear displacements, while \vec{r} and \vec{R} refer to electron and nuclear coordinates, respectively. Electronic and phonon states in the momentum space are represented by (\vec{k}, \vec{k}') and \vec{q} , respectively. Vibrational modes of crystal cause the changes in which in turn affects $\alpha^2 F$. Note also that the lattice vibrations and hence all phonon modes are already embedded in \vec{u}_i . Thus, the electron-phonon coupling [88] constant, λ , measures the average strength of the electron-phonon coupling throughout the entire phonon spectrum. Interestingly, equation(50) implies that the spectral function becomes large provided that there exists a huge equivalent set of $(\vec{k}, \vec{k}', \vec{q})$ states near the Fermi surfaces, as known as the so-called Fermi nesting [89].

The equation for T_c , as derived by McMillan [86], for weak coupling (i.e. $N_F V_{eff}$ and $\lambda \ll 1$) can be approximated to be,

$$T_c \propto \exp\left(-\frac{1}{\lambda - \mu^*}\right), \quad (51)$$

where μ^* is called the Morel-Anderson Coulomb pseudopotential parameter, accounting for repulsive effects of Coulomb interaction between electrons [88], which in general is taken as a constant. Now if equation(51) is compared with equation(47), it is clear that the BCS-based effective interaction is replaced by the difference between the electron-phonon coupling and the effective Coulomb potential: $N_F V_{eff} \rightarrow \lambda - \mu^*$ [90].

Subsequently, an improvement of the T_c equation that is capable of describing the strong coupling ($\lambda > 1$) was made by Allen and Dynes [91]. The semi-empirical formula, derived based on Eliashberg theory [92] (the full derivation of which is beyond the scope of this thesis), can be expressed as,

$$T_c = f_1 f_2 \frac{\omega_{ln}}{1.2} \exp\left[-\frac{1.04(1+\lambda)}{\lambda - \mu^*(1+0.62\lambda)}\right], \quad (52)$$

where now the Debye frequency is replaced by

$$\omega_{ln} = \exp\left(\frac{2}{\lambda} \int_0^\infty \frac{d\omega}{\omega} \ln(\omega) \alpha^2 F(\omega)\right). \quad (53)$$

Also, the strong-coupling correction factors satisfying the asymptotic behaviour of T_c are found to be,

$$f_1 f_2 = \sqrt[3]{1 + \left[\frac{\lambda}{2.46(1+3.8\mu^*)}\right]^2} \cdot \left[1 + \frac{\left(\frac{\omega_{rms}}{\omega_{ln}} - 1\right) \lambda^2}{\lambda^2 + \left(1.82(1+6.3\mu^*) \frac{\omega_{rms}}{\omega_{ln}}\right)^2}\right], \quad (54)$$

The logarithmic frequency, ω_{ln} , measures the average frequency by the aid of distribution function based on the spectral function, whereas the root-mean-square frequency is defined as

$$\omega_{rms} = \sqrt{\frac{2}{\lambda} \int_0^\infty d\omega \alpha^2 F(\omega) \omega}. \quad (55)$$

It is worth noting that when $\lambda \leq 1.5$, the strong-coupling correction factors approach unity, that is, $f_1 f_2 \approx 1$. Hence, the equation for T_c is now an explicit function of two crucial parameters, i.e. λ and ω_{ln} , both of which are dependent upon the spectral function $\alpha^2 F$. Figure 3 plots the contour profile of function T_c of equation(52) for weak coupling when $\mu^* = 0.1$.

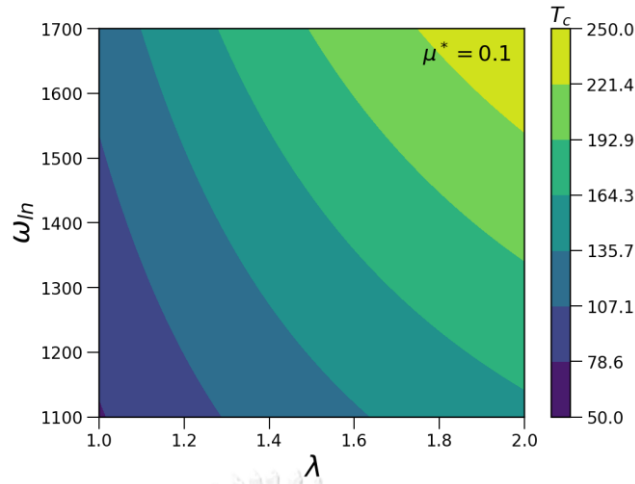


Figure 3 The contour plot of T_c equation.

2.10. The van de Waals interactions

Van de Waals (vdW) forces, also known as London dispersion forces [93], are the forces stemming from the instantaneous interaction between dipoles that are electrostatically induced by charge fluctuation. These interactions are derived from a model of two identical linear harmonic oscillators with each bearing charges $\pm e$, where the perturbed Hamiltonian of which is resulted from the corresponding Coulomb interaction of the two oscillators [94]. These interactions are of the form,

$$U(R) = -\frac{A}{R^6}, \quad (56)$$

where A is a constant, or an extended version that includes the repulsive interaction and is known as the Lennard – Jones potential [95], which is expressed as,

$$U(R) = \frac{B}{R^{12}} - \frac{A}{R^6}, \quad (57)$$

where B is another constant. Although these dispersive interactions are already in principle included in the standard exchange-correlation, these interactions are missing therein due to the inevitable approximations of E_{xc} , namely, LDA and GGA.

The first successful attempt was made by Rydberg et al [96, 97] that the exchange – correlation functional is split into two parts,

$$E_{xc}^{vdW-DF}[\rho] = E_{xc}^0[\rho] + E_c^{nl}[\rho], \quad (58)$$

with the semi-local term, $E_{xc}^0[\rho]$, is given within the Zhang and Yang reparameterization [98] of PBE of equation(92). The non-local correlation energy is expressed as,

$$E_c^{nl} = \frac{1}{2} \int d\vec{r} \int d\vec{r}' \rho(\vec{r}) \Phi(\vec{r}, \vec{r}') \rho(\vec{r}'). \quad (59)$$

Being a current subject of research, equation(59) involves an integration over electronic densities in different spatial locations that interact through a response function $\Phi(\vec{r}, \vec{r}')$ which is some given, general function depending upon $|\vec{r} - \vec{r}'|$ and the density ρ in the vicinity of \vec{r} and \vec{r}' . However, the original vdW-DF scheme is not acceptably accurate in many cases, thereby leading to alternative approaches. A second version of the van de Waals density function, or vdW-DF2 [99], had been proposed to adopt the semi-local exchange functional PW86 (which was the previous version of equation(84)) before its exchange functional was further approximated to be (called vdW-DF2-b86r) [100, 101],

$$F_x(s) = 1 + \frac{\mu s^2}{(1 + \mu s^2 / \kappa)^{4/5}}, \quad (60)$$

where μ and κ are fitted parameters that make equation(60) satisfy the GGA scheme (for a definition of s , see Appendix B). This can be further improved by taking into account the plasmon – response description for both correlation and exchange terms of vdW-DF, the enhancement of the consistent exchange vdW-DF (vdW-DF-cx) is interpolated to be of the form $F_x^{PW86r}(s)$ scaled by fractions of s^6 [102], as well as an improvement of a functional optimised from lattice constants, bulk moduli, and atomisation energies of various solids that [103] takes a formula similar to vdW-DF2-b86r. Finally, a particularly successful response function that has been proved to perform well in representative covalent, ionic, and metallic solids, takes the form [104],

$$\Phi^{rVV10} = \frac{3e^4}{2m^2} \frac{1}{(qR^2 + 1)(q'R^2 + 1)(qR^2 + q'R^2 + 2)}, \quad (61)$$

Where q and q' are defined as $\omega_0(\rho(\vec{r}), |\nabla\rho(\vec{r})|) / k(\rho(\vec{r}))$, and similarly for \vec{r}' . The

expression $\omega_0 = \sqrt{\omega_g^2 + \frac{\omega_p^2}{3}}$ comprises the plasma frequency $\omega_p^2 = \frac{4\pi\rho e^2}{m}$, the local band

gap $\omega_g^2 = 0.0093 \frac{\hbar^2}{m^2} \left| \frac{\nabla\rho}{\rho} \right|^4$ [105], and k being a function of the Thomas – Fermi screening

wave vector which controls the short-range damping of the R^{-6} .

2.11. Spin-orbit coupling

In a hydrogenic atom, the central potential that is suitable for the valence electron can no longer be defined as a pure Coulombic form. Because the electrostatic potential $\phi(\vec{r})$ presenting in

$$V_c(\vec{r}) = e\phi(\vec{r}), \quad (62)$$

no longer results only from the nucleus of charge $|e|Z$, that is, the cloud of negatively charged electrons residing in the inner shells must be taken into account. This is associated with the fact that the higher angular momentum states are prone to the repulsion due to the electronic cloud. As a consequence, a valence electron experiences the electric field, written as,

$$\vec{E} = -\frac{1}{e}\nabla V_c(\vec{r}). \quad (63)$$

However, according to electrodynamics, a moving charge subjected to an electric field will feel an effective magnetic field of,

$$\vec{B}_{eff} = -\frac{\vec{v}}{c} \times \vec{E}. \quad (64)$$

By plugging equations(62) and (63), together with the electron's magnetic dipole moment $\vec{\mu} = \frac{e\vec{S}}{m_e c}$, into the Hamiltonian of the dipole, this gives rise to,

$$H_{SOC} = -\vec{\mu} \cdot \vec{B}_{eff} = \frac{1}{2m_e^2 c^2} \frac{1}{r} \frac{dV_c}{dr} (\vec{L} \cdot \vec{S}). \quad (65)$$

A factor 2 is added because of the precession of the electronic spin moment, which is a relativistic effect when an external magnetic field is absent. The detailed derivations can be traced back to the original work proposed by L. H. Thomas [106]. The SOC Hamiltonian will be incorporated in equation(16) as a correction term.

2.12. Artificial neural network

Inspired by biological neurons, the building blocks of artificial neural networks are artificial perceptrons [107]. A single perceptron (simply called *neuron*), as illustrated in Figure 4, can be thought of as a map that takes several real inputs x_1, x_2, \dots, x_n (also called "features"),

e.g. physical properties of a material, and provides an output $y\left(\sum_i w_i x_i + b\right)$, according to

an activation function A , where the adjustable weighting $w_i \in \mathbb{R}$ and bias $b \in \mathbb{R}$ parameters are tweaked during training—just another word for fitting the model. The output of the neuron is sometimes denoted by activation, for which different possible choices are available. However, in the case of non-linear regression, the linear activation function, having the form $A = cx$, must be employed.

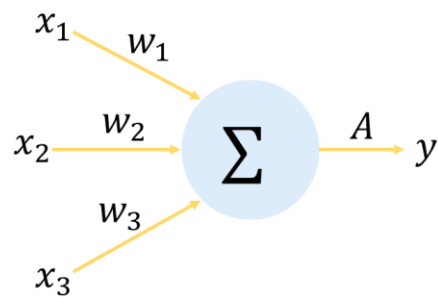


Figure 4 A typical perceptron.

Now a (feed-forward) neural network is created by arranging neurons in layers, which might perform different transformations on their features, and finally the outputs of which are determined by means of the activation of the last neuron(s) of the terminal layer [65], as schematically shown in Figure 5.

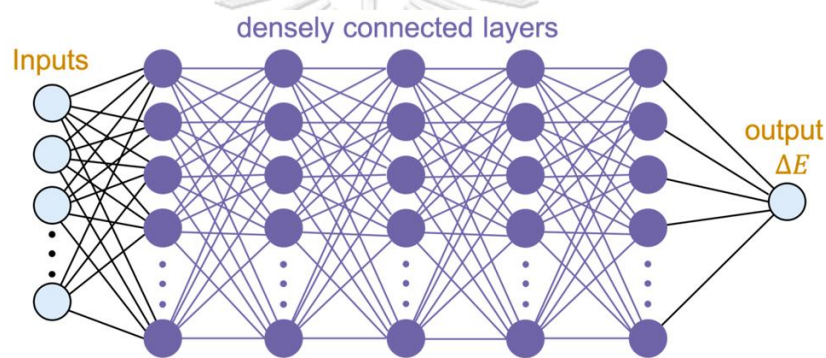


Figure 5 Fully connected feed-forward neural network.

Due to their capability to find relationships between data in high-dimensional space, neural networks can be employed to approximate any continuous function to an arbitrary accuracy given appropriate weighting parameters [108]. The model is optimised by minimising the error obtained from the model's predicted answer and the true answer based on a cost function which happens to be the root mean square error, due to its suitability for a regression task.

CHAPTER III

Superconducting $\text{Mg}_{0.5}\text{Ca}_{0.5}\text{H}_6$

3.1. Computational details

The search for the energetically favourable compositions and structures of $\text{Mg}_{0.5}\text{Ca}_{0.5}\text{H}_6$ is started off by using the Alloy-Theoretic Automated Toolkit (ATAT) to performed the cluster expansion, as implemented the Quantum Espresso (QE) package [109]. Structure variations are determined based on the corresponding formation energy obtained from the DFT calculations [110-112] with 4,000 k -point meshes, whereas the total energies and other superconducting related properties of $\text{Mg}_{0.5}\text{Ca}_{0.5}\text{H}_6$ are evaluated by the QE package [109]. The Broyden-Fletcher-Goldfarb-Shanno (BFGS) algorithm [113] with a force/atom tolerance equal to 0.001 hartree/Bohr is selected to perform the geometry optimisation of the atoms and lattice parameters. The generalised gradient approximation (GGA) method developed by Perdew-Burke-Ernzerhof (PBE) [114] is employed as the exchange-correlation functional. The plane-wave basis set with the kinetic cut-off energy and the cut-off for the charge density of 80 Ry and 320 Ry, respectively, have been tested to satisfy energy convergence. The smearing parameter, compulsory in dealing with any metallic systems since it smoothens the step and delta functions, used in all calculations is chosen to be the approximation developed by Methfessel and Paxton [115]. By using the QE package, the electron-phonon coupling (EPC) calculations are carried out with a Gaussian broadening parameter of 0.2 Ry for the integration over the Fermi surface.

3.2. Results and discussion

3.2.1. Structural stability

Equipped with the CE technique, the composition-dependent formation energies of the $\text{Mg}_{0.5}\text{Ca}_{0.5}\text{H}_6$ alloy at 200 GPa are reported in Figure 6. Some initial known structures are generated by ATAT, denoted by “Known str”, when their energies are calculated by means of DFT. Subsequently, the energy of each composition is expanded in terms of the summation of the effective cluster interaction (ECI) and their corresponding physical parameters are successively extracted. As a consequence, a large amount of (predicted) structures of different compositions are determined by evaluating equation(40). These predicted structures denoted by blue crosses. Although CE is an approximation, it would not be wrong in saying that this very technique is sufficiently efficient and reliable for a massive structure searching. Lastly, some candidates of relatively lower energy structures are selected for another round of DFT calculations to confirm their ground-state energies, as indicated by “DFT GS”.

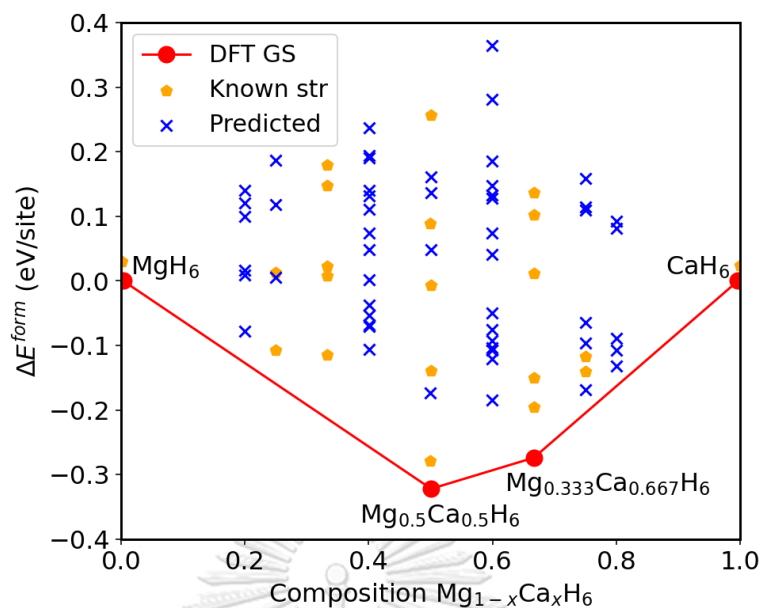


Figure 6 The formation energy in the unit of eV/atom and the corresponding convex energy hull of the $Mg_{1-x}Ca_xH_6$ at 200 GPa. Two end points account for the binary phases of MgH_6 and CaH_6 both adopting the bcc structures, as calculated from the same computational settings for comparison. The “Known str” structures are denoted by orange pentagons. The crosses indicate structures “predicted” based on the CE technique. The ground-state “DFT GS” entities are represented by red circles.

It is clear from the convex hull (Figure 6) that both $Mg_{0.5}Ca_{0.5}H_6$ and $Mg_{0.333}Ca_{0.667}H_6$ are structures with relatively lowest energies under the pressure of 200 GPa. Although these two configurations might possibly coexist in nature, the higher-symmetry $Mg_{0.5}Ca_{0.5}H_6$ is in a minimum energy state and worthwhile to be investigated. This very structure is found to be adopting an $Im\bar{3}m$ structure, where Mg/Ca atoms crystallise into a body-centred cube with a lattice parameter of 3.3215 Å, while the H atoms forming a H_{24} cage, consisting of eight H -hexagons and six H -squares, of which the Mg/Ca atoms are embedded at its centre, as illustrated in Figure 7. This structure is also known as the sodalite-like clathrate, as can be found in both MgH_6 [11] and CaH_6 [12] structures under comparable pressures. The atomic coordinates are provided in Appendix C.

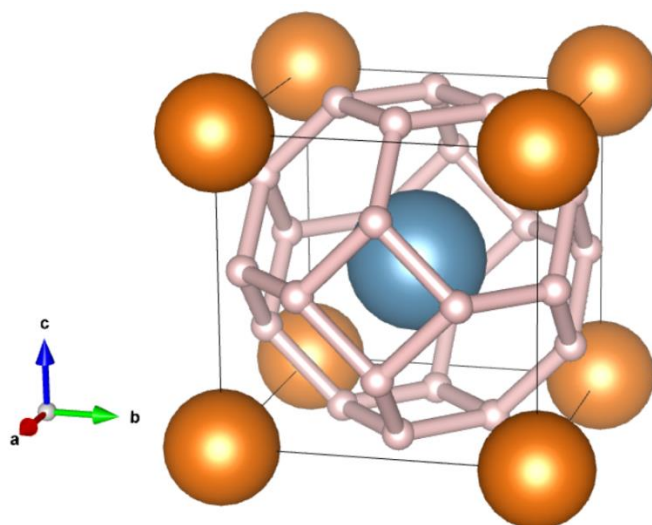


Figure 7 The body-centred cubic structure of $Mg_{0.5}Ca_{0.5}H_6$. H atoms are denoted by light pink spheres, whereas orange and blue spheres account for Mg and Ca atoms, respectively. The positions of metal atoms are interchangeable due to symmetry.

3.2.2. Electronic stability

As reported in the previous section, energies of compositions $Mg_{1-x}Ca_xH_6$ are determined, and it is noticeable that $Mg_{0.5}Ca_{0.5}H_6$ compound becomes the most favourable at 200 GPa. Concerning MgH_6 and CaH_6 (where $x=0$ and $x=1$, respectively), both structures have significantly higher energies at this very pressure. Moreover, MgH_6 was found to be unstable dynamically at 200 GPa [11].

To further investigate the corresponding electronic properties, $Mg_{0.5}Ca_{0.5}H_6$ structure is subsequently optimised by fully relaxing its atoms and lattice parameters at pressures from 200 GPa onwards, and its band structures are also calculated. The electronic band structure at the pressure of 200 GPa and the corresponding density of states (DOS) are shown in Figure 8. The band dispersion is plotted along high symmetry points defined in Figure 9.

As expected, it is blatantly metallic since there are available states for electrons highly contributed from the H atoms at the Fermi level (E_f). The total DOS at E_f , around 0.4 states per eV per formula unit (red arrow), is slightly larger than that of MgH_6 [11]. A large DOS at E_f , according to the BCS theory, leads to a high T_c value (see equation(47)).

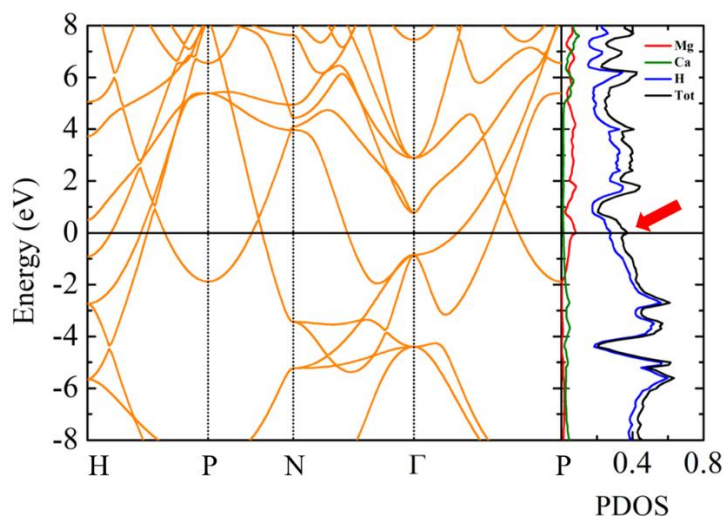
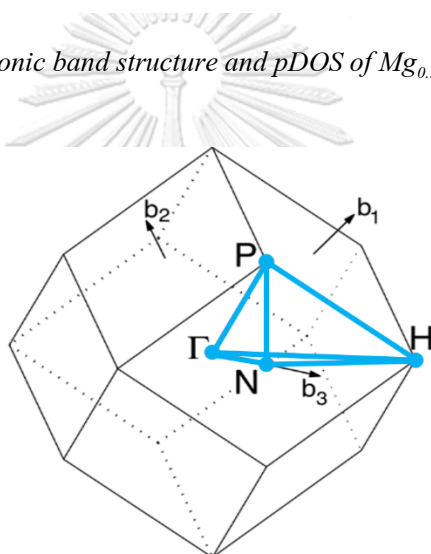


Figure 8 The electronic band structure and pDOS of $Mg_{0.5}Ca_{0.5}H_6$ at 200 GPa.



[Setyawan & Curtarolo, DOI: 10.1016/j.commatsci.2010.05.010]

Figure 9 Brillouin zone of body-centred cubic lattice [116]

At the Γ -point near the Fermi level of the $Mg_{0.5}Ca_{0.5}H_6$ metal alloy, the electronic states are predominantly occupied by the Mg – p and H bonding, similar to those of MgH_6 [11]. The states responsible for the Ca - p and H bonding situate at lower energy below the Fermi level, i.e. around -4.5 eV, compared with around -1.5 eV in CaH_6 [12]. The contributions from metal atoms are also visualised by the partial DOS (with different colours) reported in Figure 8. Interestingly, all electronic states at the Γ -point of $Mg_{0.5}Ca_{0.5}H_6$ are located at energies further down from the Fermi level, when compared with those of its parents, i.e. MgH_6 [11] and CaH_6 [12]. It is fair to say that this explains the comparative electronic stability of those on the convex hull (Figure 6). Furthermore, some electronic states near the Fermi level at the P-point, also found in MgH_6 [11], do not appear in CaH_6 [12].

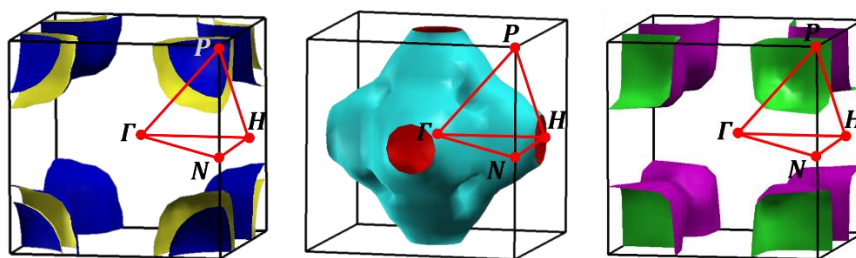


Figure 10 Fermi surfaces of $Mg_{0.5}Ca_{0.5}H_6$ at 200 GPa.

Figure 10 reports the Fermi surfaces of this metal hydride. The topology of the surfaces around the P-points in all cases is of significance in such a way that several Fermi surfaces are parallel to each other, and consequently leads to Fermi nesting, which plays a pivotal role in enhancing the electron-phonon coupling and hence superconductivity.

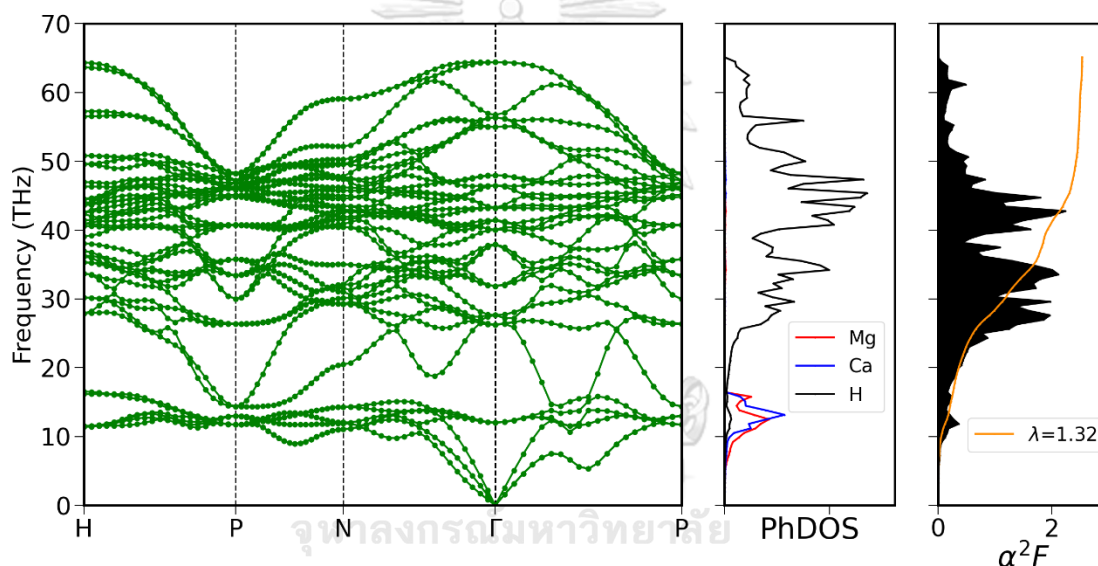


Figure 11 The calculated phonon dispersion of $Mg_{0.5}Ca_{0.5}H_6$ at 200 GPa (left); the corresponding partial phonon DOS (middle); the EPC spectral function and its cumulative EPC parameter.

3.2.3. Phonon dispersion

Obtained also from DFT, the phonon dispersion and its resulting phonon density of states (PhDOS) of $Mg_{0.5}Ca_{0.5}H_6$ under different pressures were calculated to ensure dynamical stability, as shown in Figure 11. All dispersion branches are plotted along the high-symmetry points (see Figure 11(left)), the lower frequency of which (acoustic modes) are associated with the vibrations of the heavier metal atoms, while the higher frequency of whose (optical modes) are predominantly responsible for the vibrations of the H atoms. Markedly, a number of vibrational modes of low-frequency optical phonons, between 15 – 25 THz, closely resemble those of CaH_6 at 150 GPa [12]. These very phonon modes play a crucial role

in promoting the superconducting critical temperature, T_c , as will be discussed in the next section.

From 250 GPa onwards, the mentioned low-frequency optical phonons become abruptly hardened, as there is a gap in the dispersion separating optical modes from acoustic modes. This frequency gap, the absence of PhDOS, was also found in MgH_6 at 300 GPa [11]. The variations of PhDOS of $\text{Mg}_{0.5}\text{Ca}_{0.5}\text{H}_6$ under varying pressures are reported in Figure 12.

As seen from Figure 12, it is clear that the overall phonon frequencies have a tendency to increase under elevating pressures, and is regarded as the pressure-induced phonon hardening. Specifically, the acoustic modes of *Ca* (blue) vibrate with relatively higher frequencies than those of *Mg* (red) at 200 and 250 GPa, whereas the latter outrun the former above 300 GPa. In other words, the *Ca*-associated phonon modes are softened, thereby signalling dynamical instability. Indeed, $\text{Mg}_{0.5}\text{Ca}_{0.5}\text{H}_6$ becomes dynamically unstable at pressures above 450 GPa.

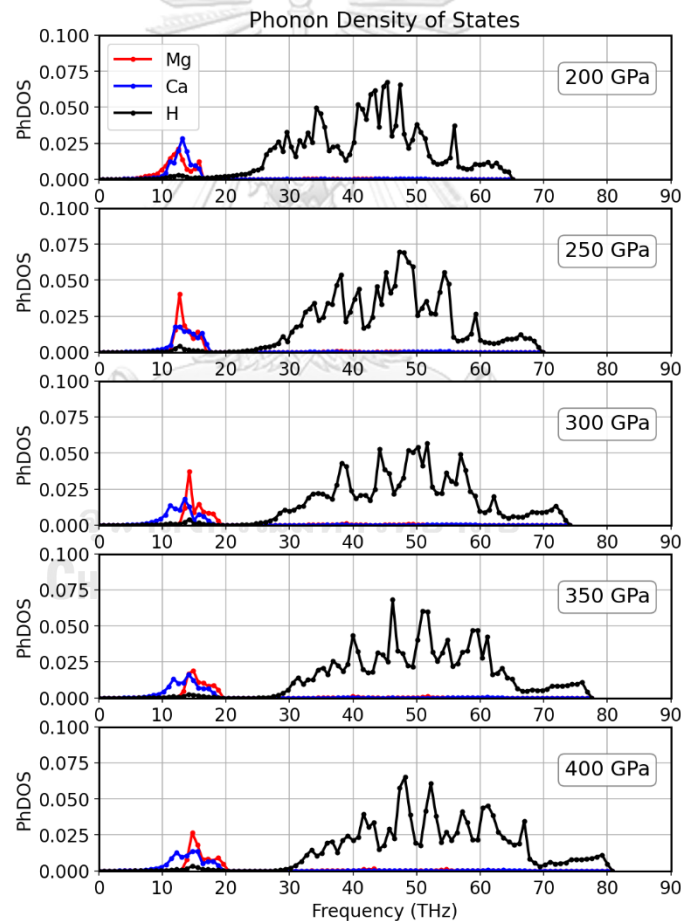


Figure 12 The calculated phonon density of states under pressures ranging from 200 to 400 GPa.

3.2.4. Spectral function and superconductivity critical temperature

Information obtained from electronic properties, such as the DOS at the Fermi level, topology of the Fermi surfaces, as well as from the phonon dispersion, e.g. Debye frequency, provides clues about superconductivity in $\text{Mg}_{0.5}\text{Ca}_{0.5}\text{H}_6$.

The spectral function $\alpha^2F(\omega)$, evaluated based on the electron-phonon coupling (EPC) matrix, of $\text{Mg}_{0.5}\text{Ca}_{0.5}\text{H}_6$ at 200 GPa is shown in Figure 11(right), when the cumulative EPC constant, which measures the average strength of EPC, is calculated by solving equation(49) and indicated as the orange line in Figure 11(right). Markedly, the slope of cumulative λ roughly changes three times. At low frequencies (0 – 15 THz), the profile is dominated by the interaction between the electrons and the acoustic (lower frequencies) phonons from the vibrations of the metal atoms, while it results from the interaction between electrons and low-frequency optical phonons at frequencies 15 – 25 THz. And clearly from 25 THz onwards, the cumulative profile is attributable to the coupling of electrons and the optical phonons of the vibrations of the H atoms. Undoubtedly, the vibrations of the H cage play a major role in affecting the strength of the EPC. Roughly speaking, λ has a linear relationship with T_c , although the correlation between the two is extremely complicated and debatable. Another crucial parameter is the logarithmic frequency ω_{\ln} , which is expressed in equation(53). This parameter measures the average EPC frequency via $\alpha^2F(\omega)$. According to equation(52), ω_{\ln} is proportional to T_c .

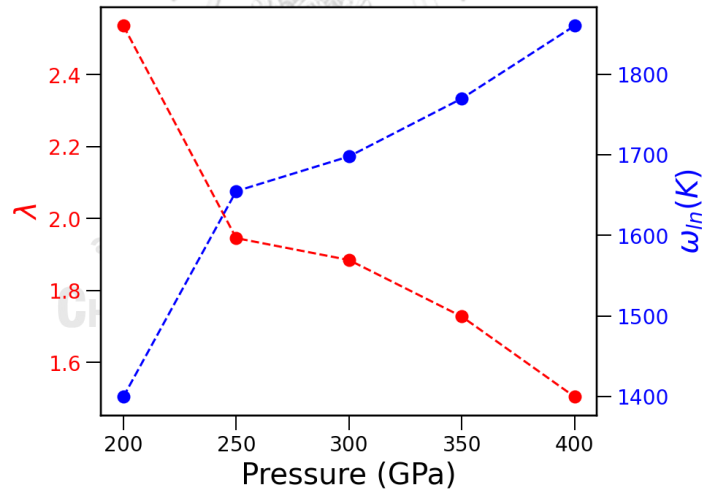


Figure 13 The EPC constant and the logarithmic frequency plotted along pressures.

Figure 13 reports the EPC constant λ and the logarithmic frequency ω_{\ln} for $\text{Mg}_{0.5}\text{Ca}_{0.5}\text{H}_6$ at varying pressures. The λ profile peaks at 2.53 at 200 GPa, when it suddenly drops to 1.94 at 250 GPa, then gradually tapers off to 1.50 at 400 GPa. On the other hand, ω_{\ln} begins at 1,400 K at 200 GPa and then shoots to 1,654 K at 250 GPa, continually increases to 1,860 K at 400 GPa. Generally speaking, it is typical in many superconducting compounds that their

λ tends to decrease as opposed to the downtrend of ω_{in} when under increasing pressures [117].

Since both behaviours of λ and ω_{in} are closely intertwined—they are not mutually independent due to the fact that each of the parameters is a function of $\alpha^2 F(\omega)$, then there is no guarantee that high values of both ω_{in} and λ will always occur at the same time. Thus, there is no harm in carrying out a deeper analysis by resorting to a simple model for the spectral function because solving for equation(50) analytically is at least impossible. The approximation of $\alpha^2 F(\omega)$ assumes that the function is constant over a frequency interval [118] (hereafter, the *bandwidth function*), as defined by,

$$\alpha^2 F(\omega) = \begin{cases} C & : \omega_1 < \omega < \omega_2 \\ 0 & : \text{elsewhere} \end{cases}. \quad (66)$$

By plugging equation(66) into equation(49):

$$\lambda = 2C \int_{\omega_1}^{\omega_2} \frac{d\omega}{\omega} = 2C \ln\left(\frac{\omega_2}{\omega_1}\right). \quad (67)$$

Similarly, for equation(53):

$$\omega_{\text{in}} = \exp\left[\frac{2C}{\lambda} \int_{\omega_1}^{\omega_2} \frac{d\omega}{\omega} \ln(\omega)\right] = \sqrt{\omega_1 \omega_2}. \quad (68)$$

The constant C is related to the average magnitude of the EPC interaction. To the best of our knowledge, ω_1 is always positive as the low-frequency vibrations of metal atoms contribute much less to $\alpha^2 F(\omega)$ when compared with the high-frequency vibrations arising from H atoms, whereas ω_2 is extended to about 70 THz (equivalent to around 3,500 K). Recall once again Figure 11(right). If $\omega_1 \approx 10$ THz and $\omega_2 \approx 65$ THz, and thus $\omega_{\text{in}} = 25.5$ THz or equivalently 1,224 K (compared with the exact value of 1,400 K). In order to find λ , the constant C needs to be specified. If C is chosen to be 0.68, then the EPC constant becomes $\lambda = 2 \times 0.68 \ln(0.65) = 2.54$. Although these expressions (equations(66), (67), and (68)) are crudely approximated, they serve as a tool that gives some insight into the behaviours of the superconductivity-related parameters. The width of the bandwidth function, i.e. $|\omega_1 - \omega_2|$, has a negative relationship with λ and ω_{in} : if it is large, λ will be large, but ω_{in} will always be smaller than ω_2 , and if it is infinitesimal, then $\omega_{\text{in}} \approx \omega_1 \approx \omega_2$, but λ will be much smaller than that of the former case. Interestingly, at the pressure of 250 GPa, there exists a frequency gap in the phonon dispersion, as discussed previously, and consequently the spectral function's profile in this gap vanishes. Now, assume that the bandwidth function is segmented into two separate pieces, i.e. that of frequency range 10 – 15 THz and that over 25 – 65 THz. Therefore, the frequency becomes $\omega_{\text{in}} = \sqrt{10 \times 15} + \sqrt{25 \times 65} \approx 52.5$ THz

or equivalently 2,520 K, which is quite distant from the exact value of 1,654, and also the EPC constant $\lambda = 2 \times 0.68 \times (\ln 1.5 + \ln 2.6) \approx 1.85$ being acceptably close to 1.94. Granted, this simple model seemingly overapproximates ω_{in} and slightly underapproximates λ , yet it clearly explains the effect of the frequency gap on λ and ω_{in} .

The superconducting critical temperature T_c is then evaluated from equation(52) with $\mu^* = 0.1$, and is plotted in Figure 14 with increasing pressures starting from 200 to 400 GPa. The ternary alloy $\text{Mg}_{0.5}\text{Ca}_{0.5}\text{H}_6$ superconducts T_c of 288 K at 200 GPa when $\lambda = 2.53$ and $\omega_{\text{in}} = 1,400$ K. The T_c profile has a tendency to decline as pressure increases, except around 250 – 300 GPa when it remains unchanged.

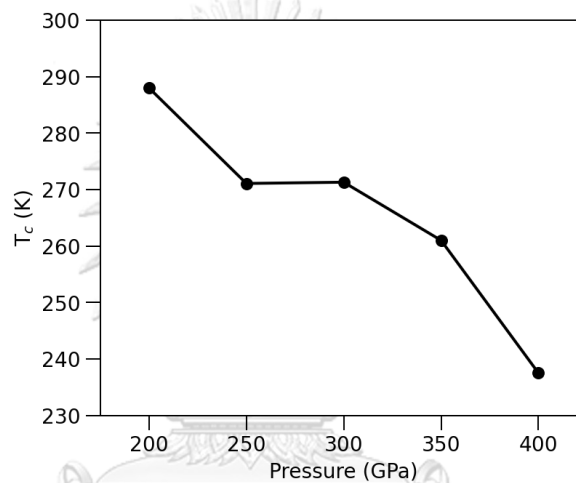


Figure 14 T_c as a function of pressure.

The behaviour of the pressure-dependent T_c poses a challenge to providing an accurate description based solely on λ and ω_{in} . However, a few points can be discussed by invoking once again the bandwidth function (equation(66)). If we plot T_c as a function of both ω_1 and ω_2 , that is, $T_c \equiv T_c(\omega_1, \omega_2)$ in Figure 15, when ω_1 and ω_2 are chosen arbitrary based on Figure 17. The model suggests that if parameter C does not vary greatly, T_c will be relatively largest when the bandwidth becomes the widest, that is, $\omega_2 \gg \omega_1$ (path A), which is line with that at 200 GPa. On the other hand, if the bandwidth is shortened (path B), T_c clearly decreases, consistent with those from 250 GPa onwards.

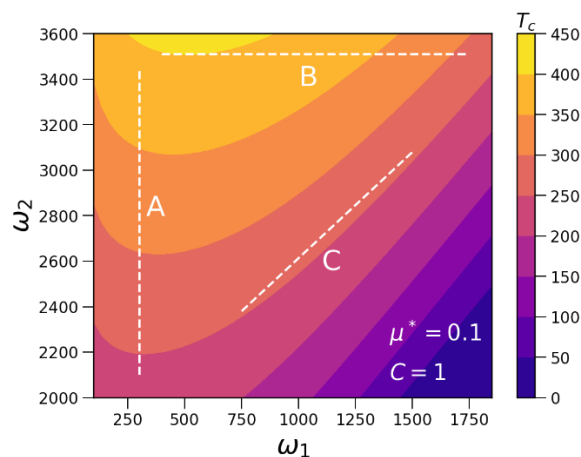


Figure 15 A contour plot of T_c as a function of ω_1 and ω_2 .

However, a special case in which the T_c profile remains constant exists in Figure 16, i.e. path C, which is in a good agreement with a plateau at 250 and 300 GPa. Indeed, the spectral function profiles at 250 and 300 GPa look somehow similar, and so the bandwidths of theirs are roughly equivalent (they can be thought of as a rigid shift) and that path C is taken.

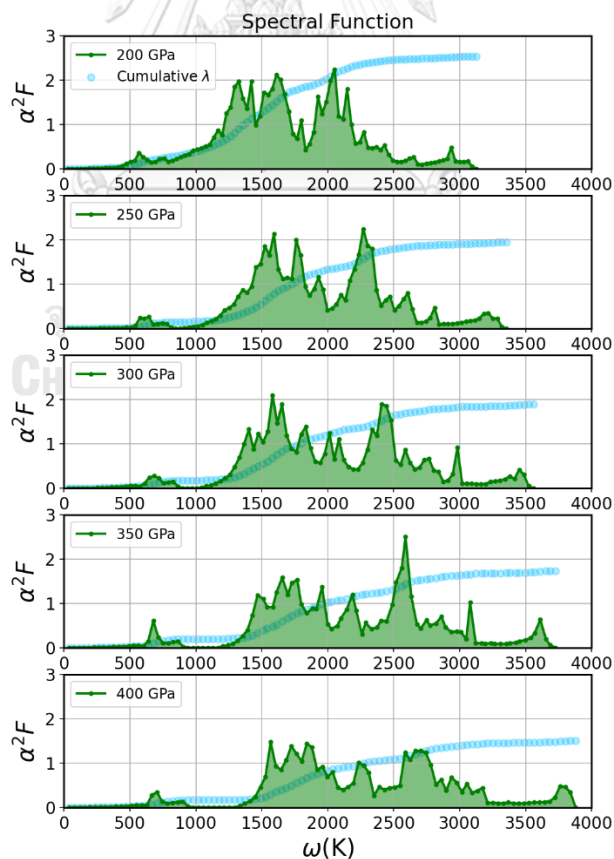


Figure 16 Spectral function of each pressure.

To this end, we discuss the role of Mg/Ca substitution. First of all, at pressure of 200 GPa the electronic band dispersion near the Fermi level is influenced by the Mg – H bonding, similar to that found in MgH₆ [11], whereas the Ca – associated states close to E_f appear to be locating at lower energies especially at Γ -point (see Figure 10), causing the Ca – H bonding to become more relatively energetically stable compared with the Mg – H bonding and some identical bonds in CaH₆ [12]. Additionally, the metal-part low-frequency phonons are situated at higher frequencies under pressures. As for CaH₆, this phonon part is limited over the range 5 – 15 THz at 200 GPa [12], while it is elevated to around 10 – 17 THz in Mg_{0.5}Ca_{0.5}H₆ at the same pressure, as can be seen in Figure 12 (left and middle). Remarkably, $\alpha^2F(\omega)$ is readjusted by the substitution of metals. It was previously reported that the strength of $\alpha^2F(\omega)$ stems from the limited frequency range 20 – 35 THz in both MgH₆ [11] and CaH₆ [12], while it is responsible for a broader frequency range 25 – 65 THz for Mg_{0.5}Ca_{0.5}H₆, as evidenced in Figure 12(right). This strength is attributable to the vibrations of the H₂₄ cage. The magnitude of $\alpha^2F(\omega)$ is slightly smaller for Mg_{0.5}Ca_{0.5}H₆ than MgH₆ [11] and CaH₆ [12], resulting in a lower λ (see Table 1 for a comparison). That being said, ω_{ln} is rather enhanced in Mg_{0.5}Ca_{0.5}H₆, comparable to its parent (isostructural) and some other similar compounds in the vicinity of 200 GPa, as high as that of MgH₆ at 300 GPa [11]. Unlike the electron-doped Li₂MgH₁₆ [10], it is fair to say that metal substitution in Mg_{0.5}Ca_{0.5}H₆ boosts phonon frequencies and optimises the strength of $\alpha^2F(\omega)$ which in turn results in a high T_c at lower pressures.

Table 1 Superconducting parameters of parent metal hydrides.

Cubic	Pressure (GPa)	λ	ω_{ln}	T_c
MgH ₆ [11]	300	3.29	1,450	263
CaH ₆ [12]	150	2.69	-	235
MgGeH ₆ [119]	200	1.16	773	66.6
CaYH ₁₂ [120]	200	2.2	1,230	196 – 248
Mg _{0.5} Ca _{0.5} H ₆ [13]	200	2.53	1,400	288

CHAPTER IV

MAPbI₃ Perovskite and vdW corrections

4.1. Computational details

Likewise, total energies and other physical properties of the cubic supercell of CH₃NH₃PbI₃ (MAPI) were thoroughly investigated using Quantum Espresso Package [109]. A simulation cell of MAPI consists of eight formula units, that is, (2×2×2 supercell of cubic phase I). The cut-off energy is tested to be 90 Ry (1,224.5 eV) as well as the unshifted *k*-point meshes gridded into 6×6×6 by Monkhorst–Pack scheme [121], both satisfy the convergence threshold of 0.021 meV/atom, thereby enabling the precise detailed examination of the difference between each MA molecular orientation. The generalised gradient approximation (GGA) developed by Perdew–Burke–Ernzerhof (PBE) [114] is used as the exchange–correlation functional. There are still, however, a number of physical phenomena that require special considerations, such as relativistic effects of *Pb* atoms, already incorporated in the PBEsol functional [122], as well as van de Waals (vdW) interaction between *H* and *I* atoms. The vdW functionals used in the work include rVV10 [104], vdW-DF [123, 124], vdW-DF2 [99], vdW-DF2-b86r [100], vdW-DF-cx [102], vdW-DF-ob86 [103] functionals. The cubic MAPI is studied as a benchmark since it is the simplest phase of which the simulation cell contains only one formula unit of the material.

In regards to the dipole configurations, the organic molecules of MA are depicted as arrows with a head *N* and a tail *C*, as shown in Figure 22. Amongst a large number of possibilities in aligning the MA cations in three-dimensional space, it is worthwhile to investigate a few extreme cases in which (1) the MA molecular orientations give a maximum total dipole moment (Scheme B) and (2) two other cases in which the total dipole moment becomes zero (Schemes A and C). Scheme B is the configuration of which the centrosymmetric property of the MA orientations is turned off [125], which in turn results in the maximum dipole moment. The centrosymmetry is perfectly achieved in Schemes A and C as the net dipole moments vanish, and the noticeable between the two cases is the orientations of the MA molecules in the spherical voids. Scheme C prohibits the dipoles to align only long the simulation cell basis vectors but to point along the <111> direction, as will be discussed later in the dipolar configurations under pressures section.

4.2. Results and discussion

4.2.1. Energy barriers

As mentioned in Introduction, the interplay between the octahedral PbI₆ tilts and the MA cationic dynamics still requires scrutiny. Suggestions have been made that the molecular dynamics of the organic cation CH₃NH₃⁺ (MA) are directly related to the rotation about the C – N axis that is achieved in average in the time scale of sub-picosecond [126].

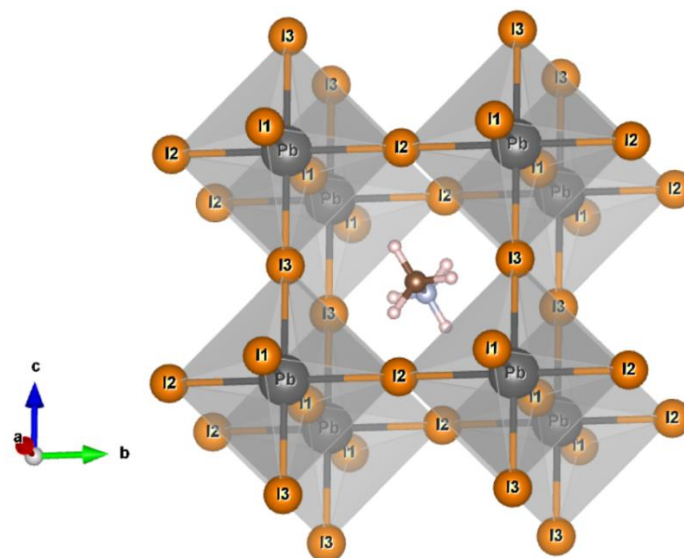


Figure 17 The cubic structure of MAPI with a lattice parameter of 6.317 Å. The MA cation consists of C (brown), N (blue), and H (pink) atoms

Besides that, the effect of the MA molecular orientations has also been proposed to play a pivotal role in determining the structure stability, as indirectly influenced by the vdW interactions, and other relevant physical properties of these hybrid organic–inorganic materials [127]. Hence, it is of significance to carry out a careful inspection of the organic – inorganic interaction by adopting PBEsol and/or with different methods that incorporate vdW dispersion, including rVV10, vdW-DF, vdW-DF2, vdW-DF2-b86r, vdW-DF-cx, vdW-DF-ob86 functionals.

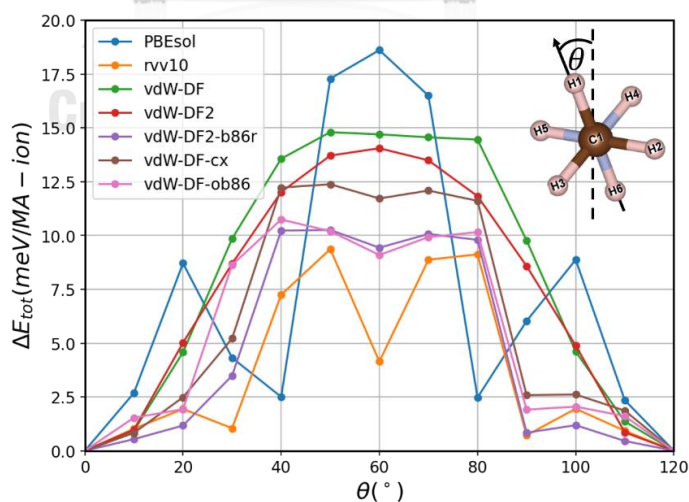


Figure 18 Total energy per cation profiles at different organic molecular orientations calculated by various functionals, when the lowest total energy is taken as a reference; Inset illustrates an applied anticlockwise rotation about the a-axis for the MA cation.

Illustrated in Figure 17, the pseudo-cubic $\text{CH}_3\text{NH}_3\text{PbI}_3$ (MAPI) of space group $\text{Im}\bar{3}$ with an average lattice parameter of 6.37 Å, consisting of an inorganic octahedral framework of PbI_6 within which embeds at its centre a dipolar organic cation of CH_3NH_3^+ that is initially chosen as a starting configuration. Owing to the C_{3v} group or the threefold symmetry, the MA cation is then applied a series of rigid rotations through an angle θ (see inset of Figure 18) that runs from 0° to 120° , as discretised into 13 steps with a 10° step size each. More importantly, all calculations are based on the assumption that the octahedral framework of PbI_6 responds quickly to the cationic rotations, and hence the whole system is fully relaxed under rotational operations.

The energy profiles at different organic orientations are reported in Figure 18, along the vertical axis of which plots the angle-dependent total energy difference per cation with the lowest one, denoted by ΔE_{tot} (meV/MA-ion). All profiles appear to be almost symmetric about $\theta = 60^\circ$ due to the 3-fold symmetry of the MA cation (see the inset). Without incorporating the vdW interaction, PBEsol functional, designed to enhance equilibrium properties of densely-packed solids [128, 129], is developed based on a fit of the exchange-correlation energy to that of the surface jellium [130]. The functional noticeably gives a distinct energy profile (blue) amongst those of the vdW functionals, specifically, at $\theta = 60^\circ$ it resembles a highest energy barrier with $\Delta E_{tot} = 18.6$ meV/MA-ion, which is flanked by a couple of smaller peaks of ~ 9 meV/MA-ion at $\theta = 20^\circ$ and $\theta = 100^\circ$. PBEsol explicitly neglects the dispersive interaction of H – I pairs that eventually entails a set of comparatively larger distances, as evidenced in Figure 19(left), and results in a highest peak at 60° . With the incorporation of vdW interactions, however, both valleys formed at $\theta = 40^\circ$ and $\theta = 80^\circ$ happen to be morphed into single broader, putatively Gaussian-like profiles. The presence of $\theta = 40^\circ$ and $\theta = 80^\circ$ -valleys is presumably stemmed from the fact that the positions of H atoms are located conveniently in an optimal level of average H – I inter-fragment distances. At $\theta = 60^\circ$, the peak prominent in PBEsol, smears out in vdW-DF (green) and vdW-DF2 (red) profiles, whereas an erosion of the peak becomes increasingly noticeable when vdW-DF-cx (brown), vdW-DF2-b86r (violet), vdW-DF-ob86 (pink), and rrv10 (orange) are performed in succession. A total energy barrier can roughly be interpreted as an entity that involves thermal excitation, i.e. $\Delta E \sim k_B T$, where ΔE denotes the flipping energy barrier [26]. The highest barrier, in our case, reads 18.6 meV/MA-ion or equivalently $T \sim 216$ K, the temperature over which the MA cation is free to randomly reorient within a void formed by octahedral PbI_6 .

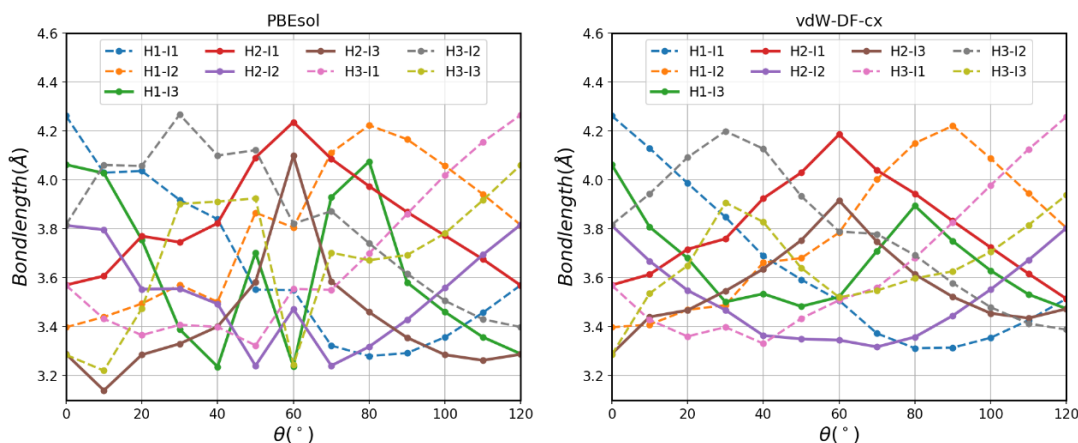


Figure 19 Different pairs of bond-lengths calculated by PBEsol and vdW-DF-cx functionals, respectively.

The overestimation of equilibrium separations and the underestimation of H–bond strengths of vdW-DF [123] which relies on the screened exchange proposed by Langreth-Vosko [131] that was later replaced by the large-N asymptote gradient correction [132], are significantly improved in vdW-DF2 [99] profile and result in a lower, unstable equilibrium peak of 21 meV/MA-ion (vdW-DF2) in lieu of the one with 1 meV/MA-ion higher peak at 60° . However, vdW-DF2-b86r, developed to improve equilibrium separations and the H–bonding in particular [100, 101] over vdW-DF2, causes a stable equilibrium at 60° as well as the one evaluated by the vdW-DF-ob86, which is reportedly suitable for hard matters [103]. More interestingly, the clearest of all peaks chiselled at 60° is obtained from the revised version of a Vydrov and van Voorhis [105] named rvv10 [104], the profile shows a distinct trend while those of other schemes display a smooth path over this angle. Finally, the total energy profile calculated by vdW-DF-cx [102], being the non-empirical functional utilising the unified vdW-DF plasmon–response representation for both correlation and exchange potentials [123], exhibits a Gaussian-like profile. Though the concavity is likely to originate from ~ 1 meV/MA-ion difference in total energy of neighbouring data points, which is smaller than energy convergence threshold set in this work. Thus, we opted for vdW-DF-cx by virtue of its pinpoint accuracy of lattice parameter predictions and H – I distances (see Figure 19(right)) [25, 102]. Nine pairs of H – I bond distances evaluated by two schemes, i.e., PBEsol and vdW-DF-cx, are plotted in Figure 19. It is well known that PBEsol explicitly disregards the dispersive interaction of H – I pairs that eventually entails a set of comparatively larger distances. Overall, the bond lengths in vdW-DF-cx scheme are significantly shortened as can clearly be seen, for example, at some apices at 60° corresponding to H2–I1, H2–I3, and H2–I2, these peaks are eroding. Interestingly, the H1–I3 profiles behave differently in both schemes, that is when dispersive interaction is taken into consideration the profile becomes smoother especially in the vicinity of $40^\circ - 80^\circ$.

4.2.2. Dipolar configurations under pressures

Increasing pressure results in a series of structural phase transitions of MAPI, the enthalpies corresponding to the cubic phase, high-pressure phase IV, and high-pressure phase V at

different pressures. The starting atomic positions are taken from Szanfranski [52]. All atoms are allowed to be fully relaxed and readjusted to confirm the possible lowest energy. The system's enthalpy as a function of pressure between 0 and 100 GPa was interpolated by the expression of 3rd-order Birch – Murnaghan equations of states [133] expressed as,

$$E(V) = E_0 + \frac{9V_0B_0}{16} \left\{ \left[\left(\frac{V_0}{V} \right)^{\frac{2}{3}} - 1 \right]^3 B'_0 + \left[\left(\frac{V_0}{V} \right)^{\frac{2}{3}} - 1 \right]^2 \left[6 - 4 \left(\frac{V_0}{V} \right)^{\frac{2}{3}} \right] \right\}. \quad (69)$$

The plots between the calculated enthalpy difference (ΔH) versus pressure corresponding to three phases of MAPI are reported in Figure 20. The inset displays the zoomed-in version of the plot indicating a small region of two-phase transitions. According to our calculations, MAPI adopts a tetragonal structure (Phase II) at ambient pressure, consistent with previously experimental reports [23, 134], while it undergoes a phase transition to Phase IV at 0.3 GPa. Finally, Phase IV morphs into Phase V at around 1.8 GPa. Compared to the previous work [52], our results are, to some extent, in a good agreement with the experimental report, though the only discrepancy at phases IV and V transition ($P = 1.8$ GPa instead of 2.5 GPa) is due to the underestimation stemming from the GGA functional. Also, our result shows that at higher pressure, the inorganic cage becomes distorted. When pressure is applied, each octahedral unit retains its shape, while the angle between the octahedra and overall atomic structure deviates from $\bar{I}m\bar{3}$ symmetry. The distortion also increases with pressure. At 0.55 GPa, the Pb–I–Pb angle is 146.78° while the same angle reduces to 144.04° at 3.83 GPa. Thus, pressure induces Pb–I distortion but not to the degree that reconstructs the original framework.

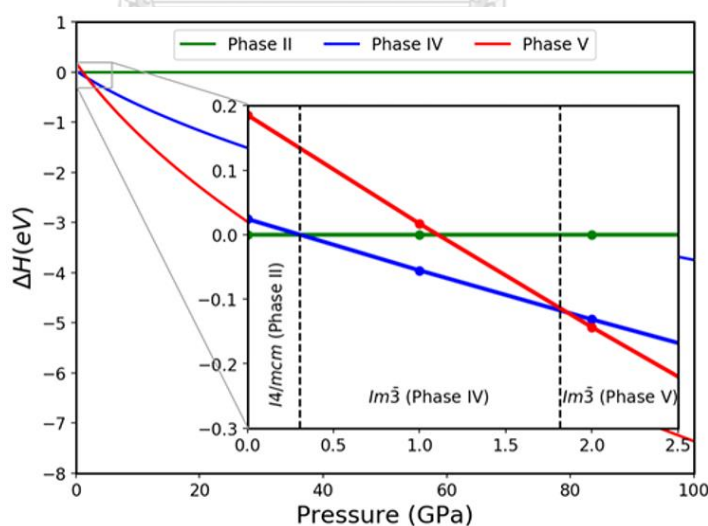


Figure 20 The relationship between enthalpy difference (eV) and pressure (GPa) calculated by vdW-DF-cx is fitted by 3rd-order Birch – Murnaghan equation of states.

In this section, the effect of dipolar orientational configurations under pressure is investigated. According to Szafranski et al [52], both phases IV and V of MAPI adopt the same space group symmetry $\text{Im}\bar{3}$, the unit cell of which is equivalent to a $2 \times 2 \times 2$ supercell expansion of the cubic phase containing 8 formula units of MAPbI_3 . Thus, there are exactly eight units of PbI_6 octahedra, eight MA cations, and eight voids available for the MA cations to occupy.

Furthermore, the voids are categorised into two types, i.e. elongated or dumbbell-like and spherical voids [52], as illustrated in Figure 21, in which the MA cation reorients itself in accordance with the shapes of the given cavity (dumbbell-like and spherical shapes in (a) and (b), respectively).

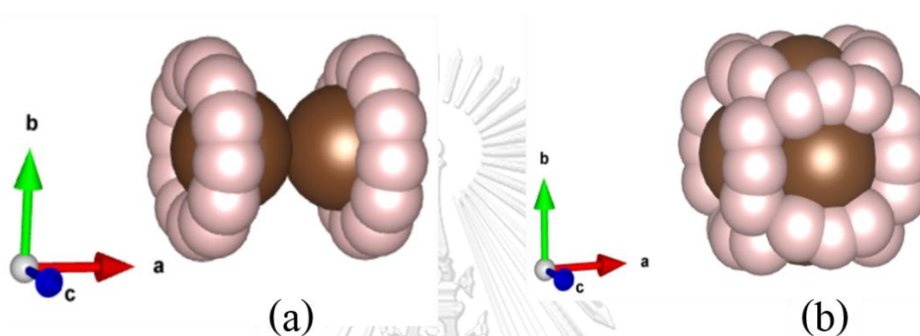


Figure 21 Two types of voids forming in MAPI. S_n denotes a spherical void; x -D, y -D, and z -D indicate dumbbell voids in their respective orientation. The MA cation in S_n (a) and x -D void (b).

Here, the molecular orientational behaviours of the MA molecule under pressures are studied, and this work's convention is introduced. Illustrated in Figure 22(a), an initial setting consists of eight cubic unit cells of MAPI, where the upper (top) accounts for $n = 2$ and the lower layer $n = 1$. A dumbbell-like void is free to realign in three possible configurations, namely, along $[100]$ ($[x-D]_n$), $[010]$ ($[y-D]_n$), and $[001]$ ($[z-D]_n$) directions, while there is an infinite possibilities in reorienting in the spherical void (S_n). The C – N dipole of the MA cation is represented by an arrow where its head corresponds to N and its tail C. Thus, there are at least two orientations in a dumbbell-like void available for the MA cation. However, there are two x -dumbbells, two y -dumbbells, two z -dumbbells and two spherical voids in the simulation cell. Therefore, there are in total at least $2^6 \times (\text{MA's alignments in a sphere})^2$ ways for the MA cation to be placed inside the voids.

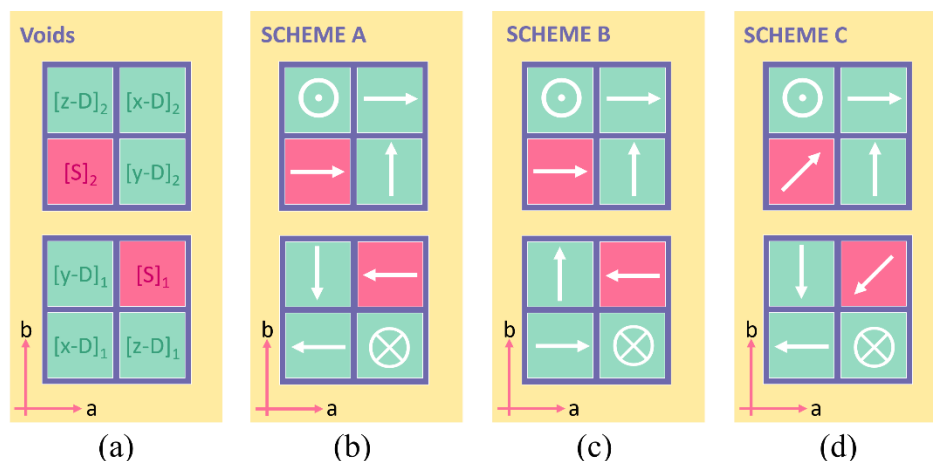


Figure 22 Schematic orientation of the CH_3NH_3 (MA) molecules. The diagram plane is in xy -plane and the lower diagrams show the bottom layer of the cell. Light red squares are the sphere voids (denoted by $[S]_n$), and green squares denote the dumbbell-like voids (denoted by $[(x, y, z)-D]_n$, where $n = 1$ indicates voids in lower layer and $n = 2$ for the upper layer of the simulation cell. Arrows/symbols in the diagrams represent the orientation of the MA molecules inside each void. The arrow head is N and the tail C. Circle \odot means that the arrow is pointing outward from the paper and the cross \otimes means that the arrow is pointing into the paper.

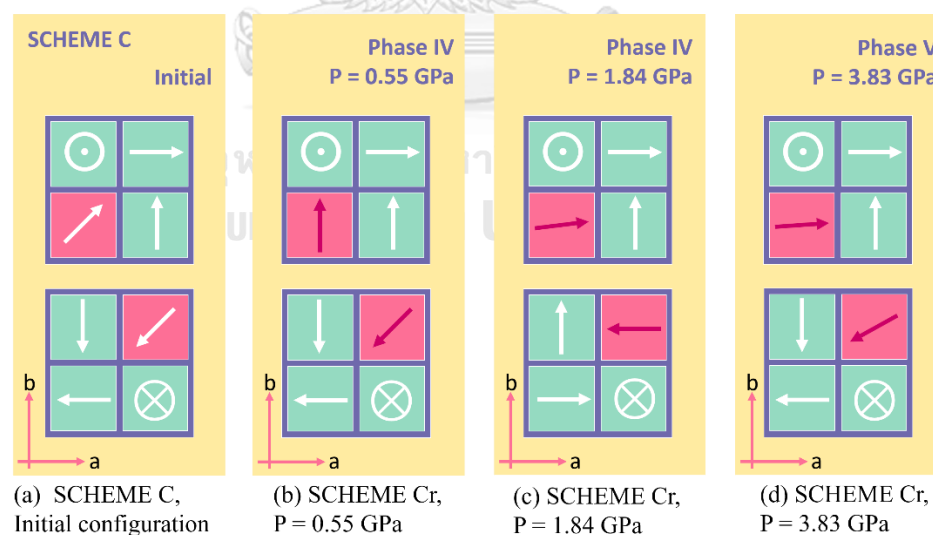


Figure 23 Schematic orientation of MA molecules. By structural optimisation starting from Scheme C in (a), the MA evolved into (b) and (c) at low pressure (0.55–2.5 GPa), and (d) at higher pressure (2.7–3.83 GPa). Cr means relaxed SCHEME C.

Amongst an almost infinite number of possibilities of how the MA cation can align, it is worthwhile to investigate only a number of extreme cases as follows:

- SCHEME A: the supercell gives zero total dipole moment.
- SCHEME B: the supercell gives maximum total dipole moment.
- SCHEME C: the supercell gives zero total dipole moment.

The difference between SCHEMES A and C, however, is the MA cation's orientations in spherical voids: MA cations point to $[111]$ and $[\bar{1}\bar{1}\bar{1}]$ directions in the latter. In the absence of pressure, the calculated unrelaxed total energies are of the relationship $A < B < C$ (see also Figure 24).

A series of structural optimisation is further performed starting with SCHEME C in which, although the net dipole moment is zero, the MA cations of $[S]_1$ and $[S]_2$ are, in fact, in an unstable equilibrium, as they have the potential to evolve into any lower energy configuration if perturbed. The configuration in SCHEME C is fully optimised by relaxing atoms and lattice under a discretised set of pressures according to the results obtained from experiments [52], i.e. 0.55, 1.84, 2.5, 2.7, and 3.83 GPa. As a result, the relaxed MA's configurations are shown in Figure 23. At low pressures, 0.55 (b) and 1.84 GPa (c), the MA molecules in the spherical voids are found to be rearranging themselves into new configurations in which the net dipole is finite but not quite large compared with that of SCHEME B.

At 0.55 GPa, remarkably, an MA cation in $[S]_1$ remains unchanged directionally as well as the others except the one in $[S]_2$ that reorients its dipole towards the *b*-axis, resulting in a finite dipole moment. However, at higher pressure the relaxed structure resembles that of SCHEME A where the net dipole almost vanishes and the MA molecules in spherical voids prefer to align with a crystal plane (*a*-axis), but when the pressure reaches 3.83 GPa, the relaxed SCHEME C adopts non-zero polarisation with an MA cation in $[S]_1$ being slightly off-centre, and that in $[S]_2$ being slightly deviated from its original orientation. Besides, the system is relatively energetically stable over the pressure range 1.8–2.5 GPa, as demonstrated by calculations of both PBEsol and vdW-DF-cx and plotted in Figure 24. Note that, though the positions of any atoms in the simulation cell are not constrained, whenever the structure adjusts to the equilibrium configuration, the MA molecules in the dumbbell-like voids are unlikely to realign themselves whatsoever. Instead they remain at least parallel to the voids in the direction they are initially placed. Thus, in MAPI crystals, the Pb-I inorganic framework has a tendency to impose a partial constraint on the organic cations.

Also, another structural optimisation of SCHEME B is carried out at pressures of 0.55 and 3.8 GPa. The configuration initially remains at minimum net dipole moment, until the MA cations in spherical voids start to deflect slightly from their original positions at low pressure. The molecules tend to avoid aligning alongside their neighbouring counterparts. Despite resulting in a highest dipole moment configuration, the structure remains in a moderate energy state that is higher than that of SCHEME A but much lower than in SCHEME C, thereby giving rise to a couple of almost invariant energy profiles in Figure 24. At 3.8 GPa, where the cell is subjected to higher pressures, the MA molecules in the spherical voids and its *c*-axis neighbours deviate. Markedly, this is the only case where the MA molecules in

dumbbell-like voids are forced to deflect away from the voids in which they situate. While the MA molecules in the spherical voids are likely to alter their positions according to the corresponding shrinkage, the MA cation in a dumbbell-like void that experiences enough repulsion from another MA cation also acts against the PbI_6 frameworks by distorting them.

As previously mentioned, the locking of organic molecules in HOIPs has been observed in both experiment and in *ab initio* molecular dynamics studies [135, 136]. Experimental studies have reported that HOIPs with large organic cations, e.g. $\text{HC}(\text{NH}_2)_2$ (FA), have longer lifetime when doped with smaller cations. One plausible explanation is that substituting smaller cations might cause the inorganic Pb–I network to distort. The distorted Pb–I network in turn constrains the movement of the larger organic cations, e.g. FA. In the case of FA molecule, the organic rotation becomes hampered due to its bent angle at the centre of the molecule [136]. However, as the MA molecules are smaller than FA and have stick-like shape with no bent angles, their rotation is less affected by the shrinkage of the void.

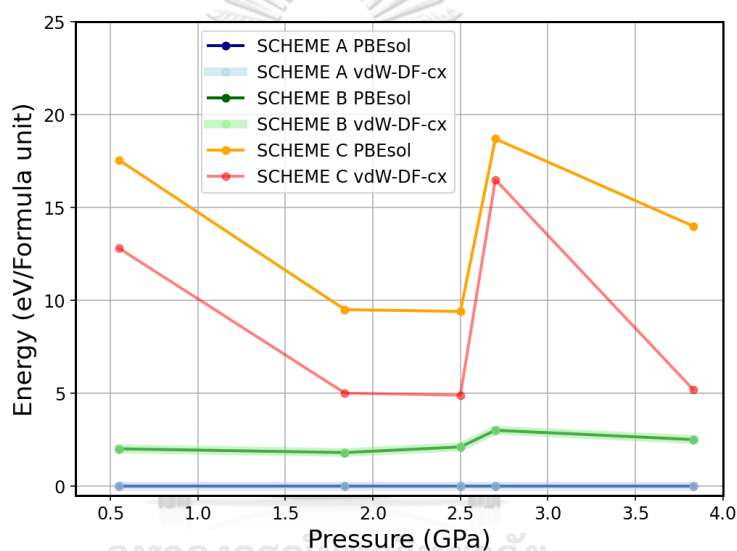


Figure 24 Energies of all schemes under pressures. Energy of SCHEME A is selected as a reference.

As the pressure is applied to MAPI, the embedded molecular voids contract and in turn inadvertently leads to stronger vdW interactions between H and I atoms. The on-axis rotation of MA is likely to enhance I_2 formation, as shown in the previous work [25]. When MA is locked into its position and unable to spin freely at high pressure, it will eventually result in a faster degradation, since Pb–I bond strength has a tendency to scale up with pressure, while the vdW interaction between I and H atoms and MA has an inverse relationship.

CHAPTER IV

MAPbI₃ perovskite and energy landscape

5.1. Computational details

In this work, all calculations are performed by the Vienna ab initio simulation package (VASP) [137]. The generalised gradient approximation (GGA) method, developed by Perdew–Burke–Ernzerhof (PBE) [114], was selected as the exchange–correlation functional. Due to the heavy *Pb* atom, the spin–orbit coupling (SOC) becomes dominant in big atoms, and is necessary to be included in all calculations. This can be done by performing self-consistent-field cycles in the non-collinear mode [138]. Also, the vdW interactions existing between H atoms and the inorganic BiSeI₂ cage requires a careful attention. Thus, the method of dispersion corrections developed by Grimme et al. (DFT-D3) [139] is used due to the presence of the organic molecule of CH₃NH₃ (MA). Nearly all data visualisations were plotted by using the Matplotlib library within Python [140].

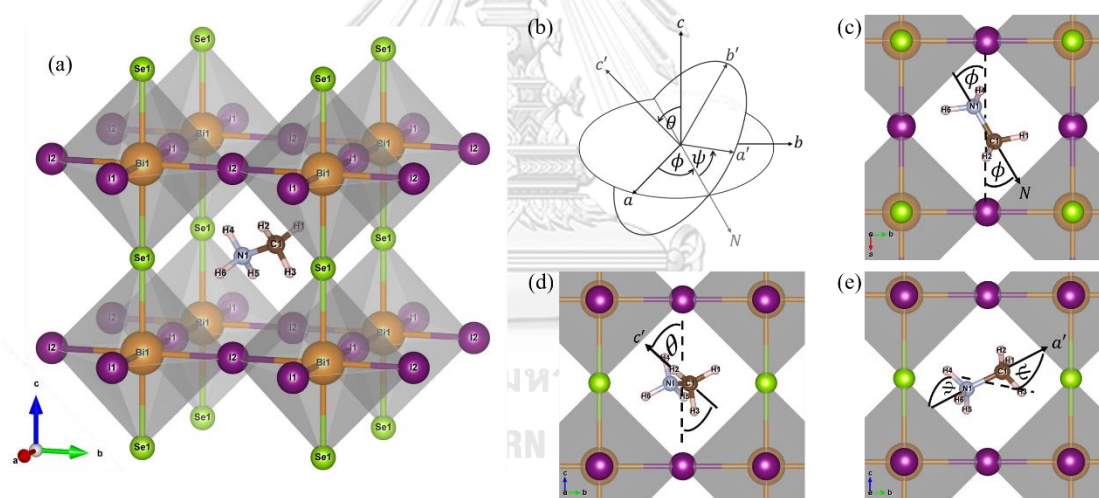


Figure 25 The cubic structure of $\text{CH}_3\text{NH}_3\text{BiSeI}_2$ (MABiSeI) with labelled atoms (a); the definition of the Euler angles (b) for the MA cation where the N–C bond is directed to the N-axis. The first rotation is rotated anticlockwise through angle ϕ about the c -axis (c). The second rotation is rotated anticlockwise via angle θ about the a' -axis or N-axis (d). Finally, the third rotation is rotated anticlockwise through angle ψ about the c' -axis (e). Note that all atoms of the inorganic BiSeI₂ cage were kept fixed throughout the calculations, while the organic MA cation was the only thing to reorient according to the Euler's rotations.

The $Pm\bar{3}m$ structure of $\text{CH}_3\text{NH}_3\text{BiSeI}_2$ or MABiSeI with a lattice constant of 6.28 Å [63] is illustrated in Figure 25(a). The initial orientation of the MA cation is arranged such that the N–C direction, denoted as the N vector, points to the centre of a cubic face (a-axis).

According to Euler's angles, the rotated coordinate, $\bar{R}' \equiv \begin{pmatrix} x' \\ y' \\ z' \end{pmatrix}$, can be evaluated from,

$$\begin{pmatrix} x \\ y \\ z \end{pmatrix} = \begin{pmatrix} \cos \psi & \sin \psi & 0 \\ -\sin \psi & \cos \psi & 0 \\ 0 & 0 & 1 \end{pmatrix} \begin{pmatrix} 1 & 0 & 0 \\ 0 & \cos \theta & \sin \theta \\ 0 & -\sin \theta & \cos \theta \end{pmatrix} \begin{pmatrix} \cos \phi & \sin \phi & 0 \\ -\sin \phi & \cos \phi & 0 \\ 0 & 0 & 1 \end{pmatrix} \begin{pmatrix} x' \\ y' \\ z' \end{pmatrix}, \quad (70)$$

where angles ϕ, θ and ψ are depicted in Figure 25(b). A series of rigid rotation is then applied to this starting cationic orientation in three-dimensional space. Under rotation, the centre of the MABiSeI 's unit cell was explicitly regarded as the origin of the body axes such that the displacement of the rigid body (the MA cation) involves no translation of the body axes. The only change is therefore in its orientations, and hence the displacements of the internal atoms of the MA cation are according to the rotation about the body axes. As illustrated in Figure 25(b-e), the Eulerian angles are performed in an anticlockwise manner starting from 0° to 345° . The molecular flips are discretised into 24 steps with a 15° step size for each angle of rotation, thereby containing $24^3 = 13,824$ sets of orientational arrangements of the MA cation, which completely cover all eight octants of the simulation cell.

5.2. Results and discussion

5.2.1. Multi-dimensional energy landscape

As previously mentioned, all other atomic positions are kept fixed except those of the MA cation that are transformed via the Eulerian angles. This is due to the fact that if the structure experiences a relaxation at every turning step, the cation can never be ensured to be in its specific orientation. For example, if the $(10^\circ, 10^\circ, 10^\circ)$ MABiSeI was structurally relaxed, then the MA cation could never point exactly along the assigned direction; it could potentially be electrostatically induced by the distorted inorganic framework [142] to point arbitrarily in the $(11.345^\circ, 9.465^\circ, 10.78^\circ)$ direction. The unrelaxed assumption is thus preferable [143]. Moreover, the molecular relaxation times of both the inorganic framework BiSeI_2 and the MA cation have yet to be observed, so it is thus hypothesised in this work that the MA cation resonates faster than the octahedral framework, which as a result is seen as stationary from the cation's perspective [26].

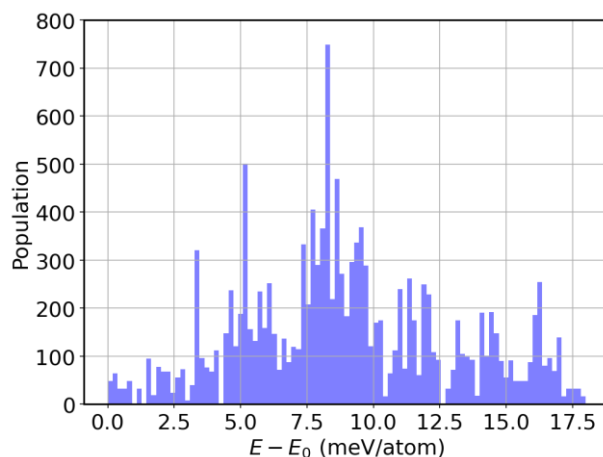


Figure 26 Energy population distribution accounting for various orientations of the MA cation, as split into 100 bins.

Figure 26 shows an energy – population distribution indicating all of the MA’s orientations for MABiSel. All total energies are normalised by subtracting each energy, E , with the lowest energy, E_0 , i.e. $E - E_0 \equiv \Delta E$. The energy distribution is truncated at the minimum and maximum of 0 and 17.9 meV/atom, respectively. The mean value, accounting for about 9 meV/atom, can be roughly thought of as an average barrier of all the MA cation’s orientation – dependent energies, depicted by the most populated array of the histograms. Moreover, the energetics can effectively be portrayed as a four-dimensional energy landscape, as shown in Figure 27, as a function of the Eulerian angles, $\Delta E \equiv \Delta E(\phi, \theta, \psi)$ [26].

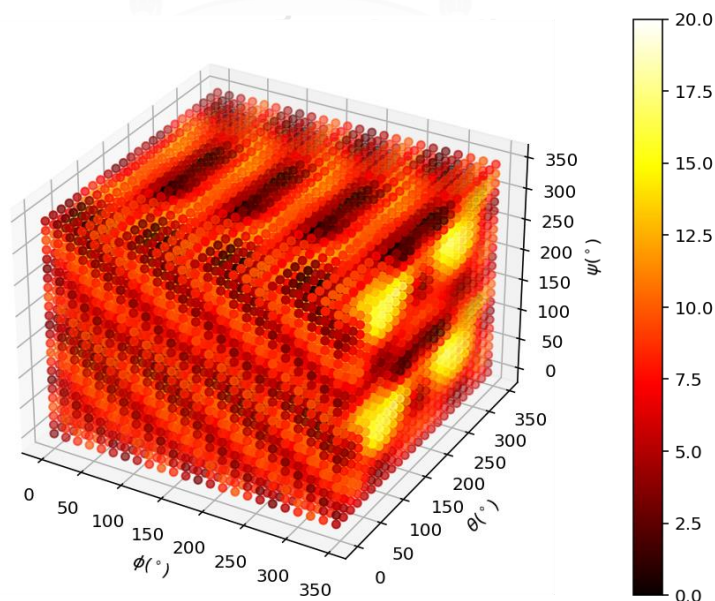


Figure 27 Four – dimensional plot of $E - E_0$ (meV/atom) with respect to the Eulerian angles.

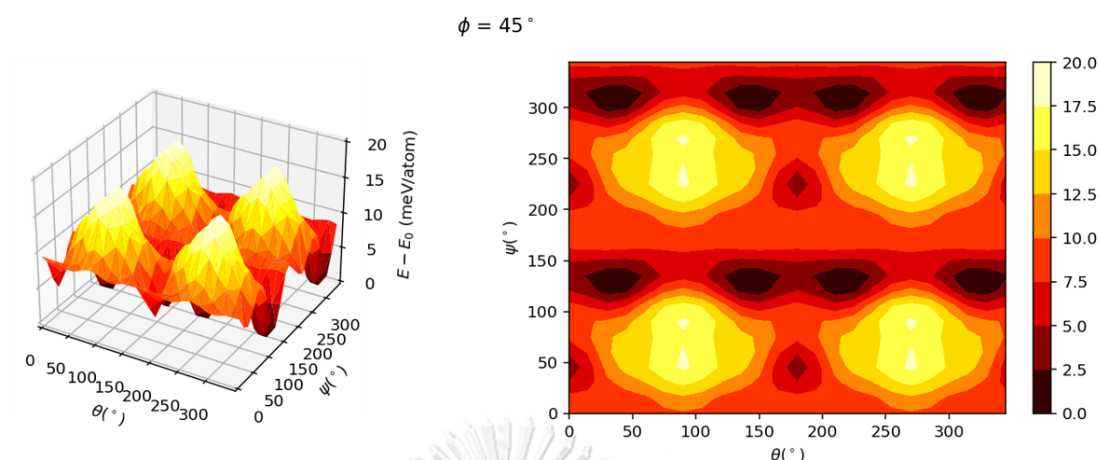


Figure 28 Three-dimensional and contour plots of $E - E_0$ with $\phi = 45^\circ$.

A series of cross-sections visualising the three-dimensional energy landscapes are discussed to preserve the orthogonality of four-dimensional axes. As an example, the geometric features of the energy landscape responsible for the MA cation orientations are illustrated by the $\Delta E(\phi = 45^\circ, \theta, \psi)$ slice, shown in Figure 28. The landscape, defined as how the organic molecule reorients within the octahedral BiSeI_2 , blatantly consists of four repeating patterns of a single hill surrounded by a couple of deep pits and a tiny cup on the left (see also the contour plot). Amongst an identical set of tallest peaks of $\Delta E = 17.9$ meV/atom, these four energy barriers—slightly smaller than those of its parent compound, i.e. FAPbI_3 (with the highest peak of 24.7 meV/atom) [26] and MAPbI_3 (18.6 meV/MA-cation) [142]. This implies that a thermal excitation energy of ~ 208 K is required to realign the MA cation according to any paths in the configurational landscape, provided that $\Delta E \sim k_B T$, where the pits indicate global minima. Markedly, further along the θ -axis from its origin in Figure 28, on the left stands a couple of the tallest mountains. By the same token, similar characteristics can be seen along the ψ -axis, but this time two global minima can be spotted. Due to these two 2D landscapes with a period of 180° , if the MA cation flips along the C–N shaft for its period, the environment remains unchanged. Also, it is worth mentioning that the 3D landscapes are geometrically reducible and thus the equivalent sets can be observed once only:

$$\Delta E(\phi, \theta, \psi) = \Delta E(\phi, 360^\circ - \theta, \psi),$$

$$\Delta E(\phi, \theta, \psi) = \Delta E(\phi + 180^\circ, \theta, \psi).$$

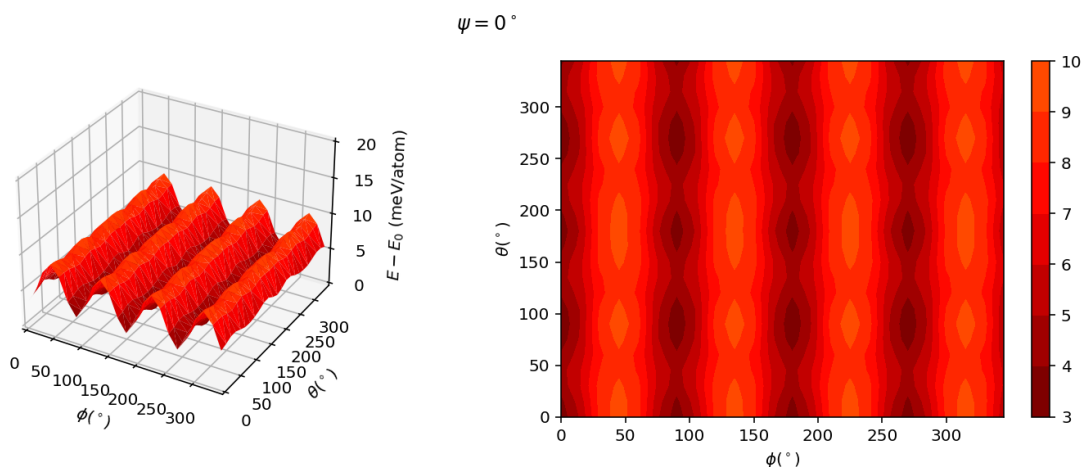


Figure 29 Energy landscape corresponding to $\psi = 0^\circ$.

If, however, one observes the landscape of a relationship between ΔE and ϕ , a Gaussian-like barrier with a 90° period can be seen, as shown in Figure 29, which is similar to that in previous reports [26, 142] with a tallest barrier of 9.6 meV/atom. The barrier in Figure 29 is attributable to the fact that the cationic dipole merely azimuthally flips from I2 to I1, and vice versa. The configurations $(\phi + n \cdot 90^\circ, \theta, 0^\circ)$ when $n = 1, \dots, 4$, resemble a set of preferred orientations according to local minima ($\Delta E = 3 - 4$ meV/atom) kept apart by arrays of saddle reefs, and the H atoms therefore are likely to point towards the I atom. Also, the ψ -fixed schemes are reducible due to the relationship $\Delta E(\phi, \theta, \psi) = \Delta E(\phi, \theta, \psi + 180^\circ)$.

5.2.2. Neural network

With the goal of learning the complicated trends and hidden correlations within a high-dimensional energy landscapes, the artificial neural network (ANN), being the famous statistical tool based on deep learning, is designed in this work using the Keras frontend on top of the Tensorflow machine learning library [144]. The model is trained by inputting, for example, the Eulerian angles (ϕ, θ, ψ) , as descriptors/features and outputting ΔE by means of regression. In general, feature augmentation reportedly plays an important role in reducing the probability of losing significant information which might improve the predictions [145]. Thus, pairwise bond lengths of those from the MA cation and the BiSel₂ framework are also included as descriptors in addition to the Eulerian angles.

Figure 5 illustrates pictorially the optimised architect of an ANN regressor comprising an input layer that is fed three Euler angles together with C – Bi, C – Se, C – I1, C – I2, H1 – Bi, H2 – Bi, and H3 – Bi bond-lengths, and is followed by five fully connected hidden layers with 500 neurons each. The output layer takes the output of the previous fully connected layer as an input and calculates the value of ΔE via a linear activation function. To train our model, 13,824 samples in our dataset are randomly sorted, as reported in Figure 30, where 80% of

the dataset is set as the training set (11,059 samples) and 20% (2,765 samples) as the test set.

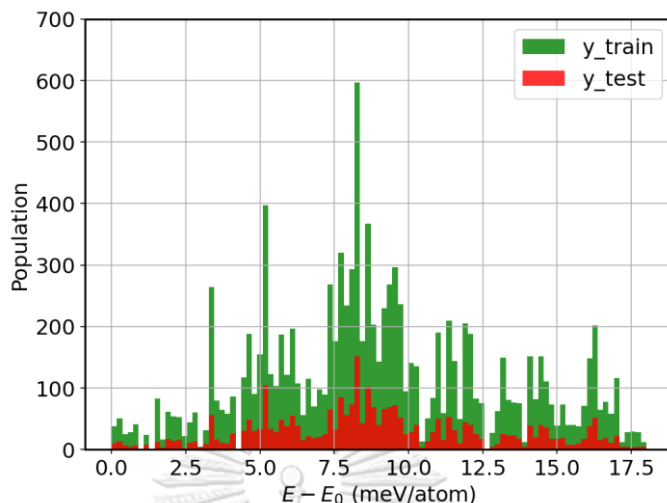


Figure 30 Training set (80% of the total samples) and test set (the other 20%) are randomly split.

The root mean square error (RMSE) between the predicted and the DFT-calculated values is selected as the cost function and is minimised during training using the Adam stochastic optimiser [146]. The dataset is normalised by subtracting the mean of each feature from each value and dividing by the feature range so that all values are within the range of 0 and 1 so as to improve the training behaviour. The training process is repeated 10 times so that the optimised values are in good agreement with a maximum 5% error.

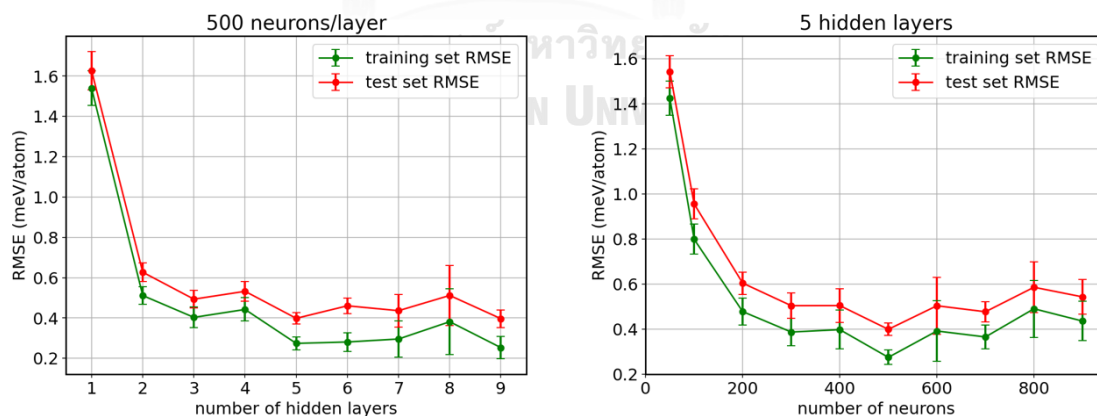


Figure 31 Variation of the RMSE of the training set (green) and test set (red) with respect to the number of hidden layers (a), and to the number of artificial neurons for each hidden layer (b).

As a result, Figure 31 report the RMSE values for varying number of hidden layers and number of neurons for each layer. Noticeably, the optimised ANN is improved upon an

increase in the number of hidden layers. Shown in Figure 31(left), the RMSEs accounting for both the training set (green) and test set (red) drop significantly at 5 hidden layers, specifically when each layer consists of 500 neurons, with which the model shows no sign of overtraining, i.e., $RMSE = 0.39 \pm 0.03$ meV/atom for the test set, while they are constantly elevated when the number of layers grows over 6 hidden layers and begin to overfit at 9 hidden layers onwards. Overfitting is uninvited because it means that the model is good at fitting the seen data but terrible at predicting unknown entities. Similarly, 500 neurons per layer for each of the five hidden layers evidently have the relatively lowest RMSE, as reported in Figure 31(right), confirming that the smallest error occurs at 500 neurons for each hidden layer.

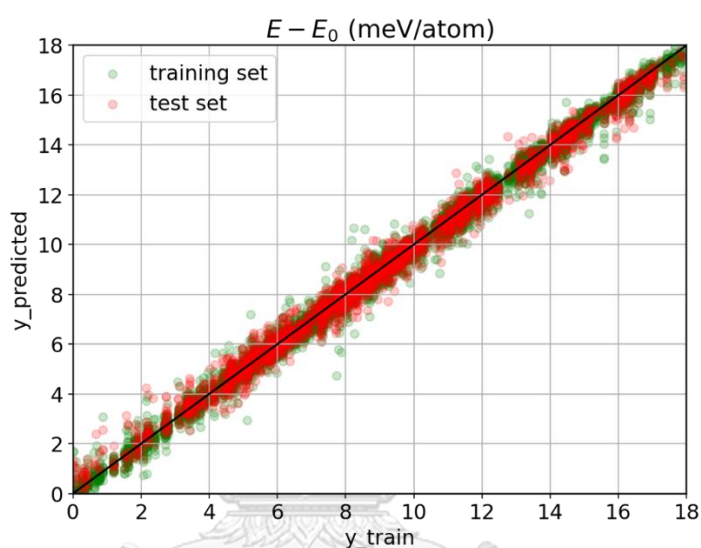


Figure 32 The predictions of the optimised ANN with 80% for training and 20% for testing, with $RMSE_{train} = 0.28$ meV/atom and $RMSE_{test} = 0.39$ meV/atom.

Figure 32 shows the results obtained from our best tweaked ANN regressor with the obtained RMSEs of 0.28 meV/atom for the training set and 0.39 meV/atom for the test set. It is clear that the proposed data-driven framework provides a reliable estimation of the DFT calculations using around 10^4 training data, together with ten descriptions of inorganic crystals as the input, by designing and systematically optimising a neural network regressor to output ΔE close to the DFT obtained values.

CHAPTER IV

Conclusions

In the first article, we have found that the $\text{Mg}_{0.5}\text{Ca}_{0.5}\text{H}_6$ ternary alloy with a clathrate structure superconducts under pressures from 200 to 400 GPa. The highest T_c of 288 K at 200 GPa are resulted from $\lambda = 2.53$ and $\omega_{\text{in}} = 1,400$ K. More recently, the superconducting metal – substituted polyhydrides, for example, Mg/Ge substitution in MgGeH_6 with $T_c \approx 67$ K and Y/Ca substitution in YCaH_{12} superconducts at $T_c \approx 215$ K, as summarised in Table 1, have attracted much attention from theorists. Also, experimental studies have been reported to successfully synthesise the Mg/Ca – substituted polyhydrides of $\text{MgCaH}_{3.72}$ and $\text{Mg}_{19}\text{Ca}_8\text{H}_{54}$ at ambient pressure and at the pressure of 2.53 GPa, respectively [147, 148]. Although these mentioned alloys do not superconduct at all, they are widely used in various advanced applications, be they hydrogen storages or switchable mirrors. These findings, including ours, would urge further experiments in search of these metal – substituted hydride superconductors.

In the second article, effects of the orientations and dipolar alignment configurations of CH_3NH_3 (MA) cations on MAPbI_3 perovskite are studied with the aid of DFT calculations. It was observed that by applying rigid azimuthal flips to the MA cation, the energy barriers calculated based on different vdW functionals exhibit distinct energy profiles and crystal structures. Three dipolar configurations are suggested and calculated using vdW-DF-cx functional under pressures. Despite being optimised under pressures, SCHEME A remains the lowest energy structure. Markedly, vdW-DF-cx and PBEsol resulted in the same amount of energy. On the other hand, the energy profiles under pressures are shifted vertically from each other in SCHEME C, even if it has zero polarisations: the vdW interaction prefers the relatively more stable energy. However, the energy profiles of both PBEsol and vdW-DF-cx functionals in SCHEME B take the second place, in spite of the fact that it is the highest polarised configuration.

As for the last article, the total energy profiles of the cubic MABiSe_2 are calculated based on the DFT calculations incorporating vdW interaction and the SOC effect. The orientational behaviours of the MA cations are described through a multi-dimensional total energy landscapes by applying the Eulerian angles to the MA cation. Several geometric slices of the three-dimensional energy landscapes exhibit local and global minima for the organic cation's orientations as well as the highest barriers of 17.9 meV per atom that protrude from the plateau of the average height of 9 meV per atom. An artificial neural network is also developed to accurately predict the total energies, with the RMSE of 0.39 meV/atom for the test dataset, by taking the Euler angles and seven sets of bond lengths as descriptors for the ANN.

Appendices

A. Energy minimisation

The Kohn-Sham equation enables us to investigate the full interacting system by mapping it with real potential onto a fictitious non-interacting system in which the electrons move within an effective KS single-particle potential.

The ground-state energy of a many-electron system are obtained by minimising the total energy functional that is subject to the constraint that conserves the number of electrons N , which can be written as,

$$\delta \left[\varepsilon[\rho(\vec{r})] - \mu \left(\int \rho(\vec{r}) d\vec{r} - N \right) \right] = 0, \quad (71)$$

which is associated with the normality constraint of each KS orbitals,

$$\sum_{i=1}^N \int \psi_i^{*KS}(\vec{r}) \psi_i^{KS}(\vec{r}) d\vec{r} = N. \quad (72)$$

Now recall the total energy functional,

$$E[\rho(\vec{r})] = T_0[\rho(\vec{r})] + \frac{1}{2} \iint \frac{\rho(\vec{r}) \rho(\vec{r}')}{|\vec{r} - \vec{r}'|} d\vec{r} d\vec{r}' + \int v_{ext}(\vec{r}) \rho(\vec{r}) d\vec{r} + E_{xc}[\rho(\vec{r})], \quad (73)$$

where the first term in equation(73), the kinetic-energy of non-interacting electron gas, is expressed as,

$$T_0[\rho(\vec{r})] = \sum_{i=1}^N \int \psi_i^{*KS}(\vec{r}) \left(-\frac{\nabla^2}{2} \right) \psi_i^{KS}(\vec{r}) d\vec{r}. \quad (74)$$

Now equation(71) becomes,

$$\frac{\delta T_0[\rho(\vec{r})]}{\delta \rho(\vec{r})} + V_{eff}(\vec{r}) = \mu, \quad (75)$$

when the effective potential is,

$$V_{eff}(\vec{r}) = V_{ext}(\vec{r}) + \int \frac{\rho(\vec{r}')}{|\vec{r} - \vec{r}'|} d\vec{r}' + V_{xc}(\vec{r}), \quad (76)$$

with the exchange-correlation potential,

$$V_{xc}(\bar{r}) = \frac{\delta E_{xc}[\rho(\bar{r})]}{\delta \rho(\bar{r})}. \quad (77)$$

Now if we rewrite equation(75) as,

$$\frac{1}{\psi_i^{*KS}(\bar{r})} \frac{\delta T_0[\rho(\bar{r})]}{\delta \psi_i^{KS}(\bar{r})} + V_{eff}(\bar{r}) = \mu, \quad (78)$$

Therefore, to solve for the ground-state energy and density, all that has to be done is solve the one-electron equation,

$$\left[-\frac{1}{2} \nabla_i^2 + V_{eff}(\bar{r}) \right] \psi_i^{KS}(\bar{r}) = E \psi_i^{KS}(\bar{r}). \quad (79)$$

Now to derive the Hartree term in equation(76), recall the Hartree energy,

$$J[\rho(\bar{r})] = \frac{1}{2} \iint \frac{\rho(\bar{r})\rho(\bar{r}')}{|\bar{r} - \bar{r}'|} d\bar{r}d\bar{r}'. \quad (80)$$

According to the variation principle, the minimisation is performed where $\phi(\bar{r})$ is an arbitrary function:

$$\begin{aligned} \frac{\delta J[\rho(\bar{r})]}{\delta \rho(\bar{r})} \phi(\bar{r}) d\bar{r} &= \left[\frac{d}{d\varepsilon} J[\rho(\bar{r}) + \varepsilon \phi(\bar{r})] \right]_{\varepsilon=0} \\ &= \left[\frac{d}{d\varepsilon} \frac{1}{2} \iint \frac{[\rho(\bar{r}) + \varepsilon \phi(\bar{r})][\rho(\bar{r}') + \varepsilon \phi(\bar{r}')] }{|\bar{r} - \bar{r}'|} d\bar{r}d\bar{r}' \right]_{\varepsilon=0} \\ &= \frac{1}{2} \iint \frac{\rho(\bar{r}') \phi(\bar{r})}{|\bar{r} - \bar{r}'|} d\bar{r}d\bar{r}' + \frac{1}{2} \iint \frac{\rho(\bar{r}) \phi(\bar{r}')}{|\bar{r} - \bar{r}'|} d\bar{r}d\bar{r}'. \end{aligned} \quad (81)$$

And since \bar{r} and \bar{r}' are interchangeable, we thus have the variation of the Hartree energy expressed as,

$$\frac{\delta J[\rho(\bar{r})]}{\delta \rho(\bar{r})} = \frac{1}{2} \int \frac{\rho(\bar{r}')}{|\bar{r} - \bar{r}'|} d\bar{r}'. \quad (82)$$

B. The generalised gradient approximation

Perdew et al [149] made vital steps by devising a cut-off procedure that sharply truncates the gradient expansion approximation exchange-correlation hole in real-space by means of delta function, for the purpose of restoring the sum rule and non-positivity hole conditions. As a result, one the GGA can now be written as,

$$E_{xc}^{GGA}[\rho(\bar{r})] = \int d\bar{r} \rho(\bar{r}) \varepsilon_{xc}^{\text{hom}}[\rho(\bar{r})] \cdot F_{xc}[\rho(\bar{r}), \nabla \rho(\bar{r})]. \quad (83)$$

A crucial GGA functional used widely and frequently by the DFT community is that belonging to Perdew and Wang, also known as PW91 [150, 151]. The non-empirical PW91 are defined with the exchange enhancement factor having the form,

$$F_x^{PW91}(s) = \frac{1 + 0.19645s \sinh^{-1}(7.7956s) + (0.2743 - 0.15084e^{-100s^2})s^2}{1 + 0.19645s \sinh^{-1}(7.7956s) + 0.004s^4}, \quad (84)$$

with the dimensionless reduced density gradient defined as,

$$s(\vec{r}) = \frac{|\nabla\rho(\vec{r})|}{2k_F(\vec{r})\rho(\vec{r})}, \quad (85)$$

and the Fermi-wavevector,

$$k_F(\vec{r}) = \sqrt[3]{3\pi^2\rho(\vec{r})}. \quad (86)$$

The PW91 correlation can be written in terms of the Seitz radius r_s as,

$$E_c^{PW91}[\rho_\alpha, \rho_\beta] = \int \rho(\vec{r}) [\varepsilon_c(r_s, \zeta) + H(t, r_s, \zeta)] d\vec{r}, \quad (87)$$

where $\varepsilon_c(r_s, \zeta)$ denotes the parametrisation of the homogeneous electron gas correlation energy [152], and also another dimensionless gradient term

$$t = \frac{|\nabla\rho(\vec{r})|}{\left[(1+\zeta)^{2/3} + (1-\zeta)^{2/3} \right] \cdot \sqrt{\frac{4k_F}{\pi}} \cdot \rho(\vec{r})}. \quad (88)$$

ζ indicates the degree of spin-polarisation. Now the function $H = H_0 + H_1$, is defined as,

$$\begin{aligned} H_0 &= g^3 \frac{\beta^2}{2\alpha} \log \left[1 + \frac{2\alpha}{\beta} \left(\frac{t^2 + At^4}{1 + At^2 + A^2t^4} \right) \right], \\ H_1 &= \nu \left[C_c(r_s) - C_c(0) - \frac{3}{7} C_x \right] g^3 t^2 \exp \left[-100g^4 \left(\frac{k_s^2}{k_F^2} \right) t^2 \right], \\ A &= \frac{2\alpha}{\beta} \left(e^{\frac{2\alpha\varepsilon}{g^3\beta^2}} - 1 \right), \end{aligned} \quad (89)$$

with $\alpha = 0.09$, $\beta = \nu C(0)$, $\nu = \frac{16}{\pi} \sqrt[3]{3\pi^2} = 0.004235$, $C_x = -0.001667$. According to

Rasolt and Geldart [153], C_x is given by,

$$C_c(r_s) = 10^{-3} \left(\frac{2.568 + ar_s + br_s^2}{1 + cr_s + dr_s^2 + 10br_s^3} \right) - C_x, \quad (90)$$

with

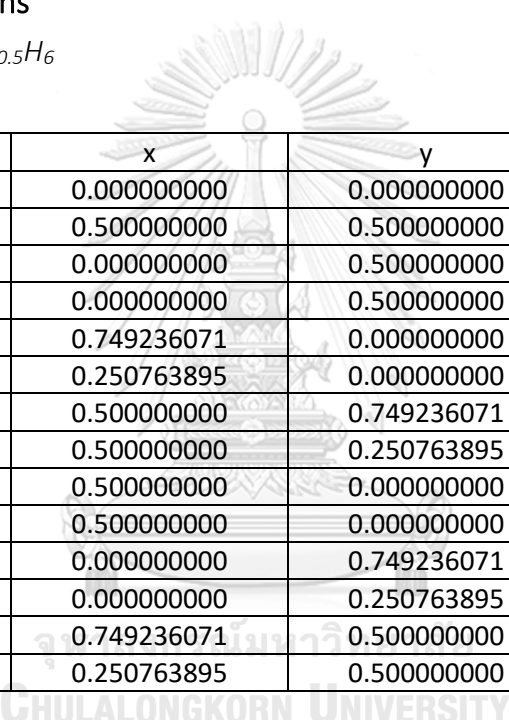
$$a = 23.266, b = 7.389 \times 10^{-3}, c = 8.723, d = 0.472. \quad (91)$$

The role of $H(t, r_s, \zeta)$ is governed by the correlation hole's behaviour in the limit of high density [154, 155]. Until very recently, PW91 has been now superseded by a modified version by Perdew, Burke, and Ernzerhof (PBE) [114], which is defined as an extremely simpler exchange enhancement factor of the form:

$$F_x^{PBE}(s) = 1.804 - \frac{0.804}{1 + 0.273s^2}. \quad (92)$$

C. Atomic positions

i. $Mg_{0.5}Ca_{0.5}H_6$



Atoms	x	y	z
Mg	0.000000000	0.000000000	0.000000000
Ca	0.500000000	0.500000000	0.500000000
H	0.000000000	0.500000000	0.749236071
H	0.000000000	0.500000000	0.250763895
H	0.749236071	0.000000000	0.500000000
H	0.250763895	0.000000000	0.500000000
H	0.500000000	0.749236071	0.000000000
H	0.500000000	0.250763895	0.000000000
H	0.500000000	0.000000000	0.250763895
H	0.500000000	0.000000000	0.749236071
H	0.000000000	0.749236071	0.500000000
H	0.000000000	0.250763895	0.500000000
H	0.749236071	0.500000000	0.000000000
H	0.250763895	0.500000000	0.000000000

ii. $MAPbI_3$

Atoms	x	y	z
C	0.596942021	0.491789987	0.499962968
N	0.361402991	0.491789987	0.499962968
H1	0.655720032	0.656453968	0.499962968
H2	0.652230951	0.408840010	0.643757040
H3	0.652379008	0.408363988	0.356516015
H4	0.299060995	0.566852992	0.634274022
H5	0.299211004	0.566469021	0.365063005
H6	0.296755020	0.338210032	0.500002992
I1	0.500000000	0.000000000	0.000000000
I2	0.000000000	0.500000000	0.000000000
I3	0.000000000	0.000000000	0.500000000
Pb	0.000000000	0.000000000	0.000000000

iii. $MABiSeI_2$

Atoms	x	y	z
C	0.596942021	0.491789987	0.499962968
N	0.361402991	0.491789987	0.499962968
H1	0.655720032	0.656453968	0.499962968
H2	0.652230951	0.408840010	0.643757040
H3	0.652379008	0.408363988	0.356516015
H4	0.299060995	0.566852992	0.634274022
H5	0.299211004	0.566469021	0.365063005
H6	0.296755020	0.338210032	0.500002992
Bi	0.000000000	0.000000000	0.000000000
I1	0.500000000	0.000000000	0.000000000
I2	0.000000000	0.500000000	0.000000000
Se	0.000000000	0.000000000	0.500000000



REFERENCES

1. Hafemeister, D.W., *Review of Sustainable Energy—Without the Hot Air by David MacKay*. American Journal of Physics, 2010. **78**(2): p. 222.
2. Onnes, H.K. *Further experiments with liquid helium. C. On the change of electric resistance of pure metals at very low temperatures etc. IV. The resistance of pure mercury at helium temperatures.* in *KNAW, Proceedings*. 1911.
3. Bardeen, J., L.N. Cooper, and J.R. Schrieffer, *Theory of superconductivity*. Physical review, 1957. **108**(5): p. 1175.
4. Nagamatsu, J., et al., *Superconductivity at 39 K in magnesium diboride*. nature, 2001. **410**(6824): p. 63-64.
5. Duan, D., et al., *Pressure-induced metallization of dense (H₂S)₂H₂ with high-T_c superconductivity*. Scientific Reports, 2014. **4**(1): p. 6968.
6. Drozdov, A., et al., *Conventional superconductivity at 203 kelvin at high pressures in the sulfur hydride system*. Nature, 2015. **525**(7567): p. 73-76.
7. Liu, H., et al., *Potential high-T_c superconducting lanthanum and yttrium hydrides at high pressure*. Proceedings of the National Academy of Sciences, 2017. **114**(27): p. 6990-6995.
8. Peng, F., et al., *Hydrogen clathrate structures in rare earth hydrides at high pressures: possible route to room-temperature superconductivity*. Physical review letters, 2017. **119**(10): p. 107001.
9. Somayazulu, M., et al., *Evidence for superconductivity above 260 K in lanthanum superhydride at megabar pressures*. Physical review letters, 2019. **122**(2): p. 027001.
10. Sun, Y., et al., *Route to a superconducting phase above room temperature in electron-doped hydride compounds under high pressure*. Physical review letters, 2019. **123**(9): p. 097001.
11. Feng, X., et al., *Compressed sodalite-like MgH₆ as a potential high-temperature superconductor*. RSC advances, 2015. **5**(73): p. 59292-59296.
12. Wang, H., et al., *Superconductive sodalite-like clathrate calcium hydride at high pressures*. Proceedings of the National Academy of Sciences, 2012. **109**(17): p. 6463-6466.
13. Sukmas, W., et al., *Near-room-temperature superconductivity of Mg/Ca substituted metal*

- hexahydride under pressure*. Journal of Alloys and Compounds, 2020. **849**: p. 156434.
14. Williams, M. *What is the Life Cycle Of The Sun?* 2015; Available from:
<https://www.universetoday.com/18847/life-of-the-sun/>
 15. Parida, B., S. Iniyar, and R. Goic, *A review of solar photovoltaic technologies*. Renewable and sustainable energy reviews, 2011. **15**(3): p. 1625-1636.
 16. Park, N.-G., *Perovskite solar cells: an emerging photovoltaic technology*. Materials today, 2015. **18**(2): p. 65-72.
 17. Zhou, H., et al., *Interface engineering of highly efficient perovskite solar cells*. Science, 2014. **345**(6196): p. 542-546.
 18. Brenner, T.M., et al., *Hybrid organic–inorganic perovskites: low-cost semiconductors with intriguing charge-transport properties*. Nature Reviews Materials, 2016. **1**(1): p. 1-16.
 19. Green, M.A., A. Ho-Baillie, and H.J. Snaith, *The emergence of perovskite solar cells*. Nature photonics, 2014. **8**(7): p. 506-514.
 20. Berry, J., et al., *Hybrid organic–inorganic perovskites (HOIPs): Opportunities and challenges*. Advanced Materials, 2015. **27**(35): p. 5102-5112.
 21. Mitzi, D.B., et al., *Conducting tin halides with a layered organic-based perovskite structure*. Nature, 1994. **369**(6480): p. 467-469.
 22. Frost, J.M., et al., *Atomistic origins of high-performance in hybrid halide perovskite solar cells*. Nano letters, 2014. **14**(5): p. 2584-2590.
 23. Weller, M.T., et al., *Complete structure and cation orientation in the perovskite photovoltaic methylammonium lead iodide between 100 and 352 K*. Chemical communications, 2015. **51**(20): p. 4180-4183.
 24. Bechtel, J.S., R. Seshadri, and A. Van der Ven, *Energy landscape of molecular motion in cubic methylammonium lead iodide from first-principles*. The Journal of Physical Chemistry C, 2016. **120**(23): p. 12403-12410.
 25. Klinkla, R., et al., *The crucial role of density functional nonlocality and on-axis CH₃NH₃ rotation induced I₂ formation in hybrid organic-inorganic CH₃NH₃PbI₃ cubic perovskite*. Scientific Reports, 2018. **8**(1): p. 13161.

26. Sukmas, W., et al., *Organic molecule orientations and Rashba–Dresselhaus effect in α -formamidinium lead iodide*. The Journal of Physical Chemistry C, 2019. **123**(27): p. 16508-16515.
27. Yang, Y. and J. You, *Make perovskite solar cells stable*. Nature News, 2017. **544**(7649): p. 155.
28. Saliba, M., et al., *Incorporation of rubidium cations into perovskite solar cells improves photovoltaic performance*. Science, 2016. **354**(6309): p. 206-209.
29. Yang, W.S., et al., *High-performance photovoltaic perovskite layers fabricated through intramolecular exchange*. Science, 2015. **348**(6240): p. 1234-1237.
30. Yang, W.S., et al., *Iodide management in formamidinium-lead-halide-based perovskite layers for efficient solar cells*. Science, 2017. **356**(6345): p. 1376-1379.
31. McMeekin, D.P., et al., *A mixed-cation lead mixed-halide perovskite absorber for tandem solar cells*. Science, 2016. **351**(6269): p. 151-155.
32. Correa-Baena, J.-P., et al., *The rapid evolution of highly efficient perovskite solar cells*. Energy & Environmental Science, 2017. **10**(3): p. 710-727.
33. Manser, J.S., et al., *Making and breaking of lead halide perovskites*. Accounts of chemical research, 2016. **49**(2): p. 330-338.
34. Shahbazi, M. and H. Wang, *Progress in research on the stability of organometal perovskite solar cells*. Solar Energy, 2016. **123**: p. 74-87.
35. Pathak, S., et al., *Atmospheric influence upon crystallization and electronic disorder and its impact on the photophysical properties of organic–inorganic perovskite solar cells*. ACS nano, 2015. **9**(3): p. 2311-2320.
36. Zhang, F., et al., *Perovskite $\text{CH}_3\text{NH}_3\text{PbI}_3-x\text{Br}_x$ Single Crystals with Charge-Carrier Lifetimes Exceeding 260 μs* . ACS applied materials & interfaces, 2017. **9**(17): p. 14827-14832.
37. Grancini, G., et al., *One-Year stable perovskite solar cells by 2D/3D interface engineering*. Nature communications, 2017. **8**(1): p. 1-8.
38. Wang, Y., et al., *Density functional theory analysis of structural and electronic properties of orthorhombic perovskite $\text{CH}_3\text{NH}_3\text{PbI}_3$* . Physical Chemistry Chemical Physics, 2013. **16**(4): p. 1424-1429.

39. Egger, D.A. and L. Kronik, *Role of dispersive interactions in determining structural properties of organic–inorganic halide perovskites: insights from first-principles calculations*. The journal of physical chemistry letters, 2014. **5**(15): p. 2728-2733.
40. Lee, J.H., et al., *The nature of hydrogen-bonding interaction in the prototypic hybrid halide perovskite, tetragonal CH₃NH₃PbI₃*. Scientific reports, 2016. **6**(1): p. 1-12.
41. El-Mellouhi, F., et al., *Hydrogen bonding and stability of hybrid organic–inorganic perovskites*. ChemSusChem, 2016. **9**(18): p. 2648-2655.
42. Saliba, M., et al., *Cesium-containing triple cation perovskite solar cells: improved stability, reproducibility and high efficiency*. Energy & environmental science, 2016. **9**(6): p. 1989-1997.
43. Yun, J.S., et al., *Critical role of grain boundaries for ion migration in formamidinium and methylammonium lead halide perovskite solar cells*. Advanced Energy Materials, 2016. **6**(13): p. 1600330.
44. Shockley, W. and H.J. Queisser, *Detailed balance limit of efficiency of p–n junction solar cells*. Journal of applied physics, 1961. **32**(3): p. 510-519.
45. Knutson, J.L., J.D. Martin, and D.B. Mitzi, *Tuning the band gap in hybrid tin iodide perovskite semiconductors using structural templating*. Inorganic chemistry, 2005. **44**(13): p. 4699-4705.
46. Brivio, F., A.B. Walker, and A. Walsh, *Structural and electronic properties of hybrid perovskites for high-efficiency thin-film photovoltaics from first-principles*. Apl Materials, 2013. **1**(4): p. 042111.
47. Amat, A., et al., *Cation-induced band-gap tuning in organohalide perovskites: interplay of spin–orbit coupling and octahedra tilting*. Nano letters, 2014. **14**(6): p. 3608-3616.
48. Kumawat, N.K., et al., *Structural, optical, and electronic properties of wide bandgap perovskites: Experimental and theoretical investigations*. The Journal of Physical Chemistry A, 2016. **120**(22): p. 3917-3923.
49. Wang, Y., et al., *Pressure-induced phase transformation, reversible amorphization, and anomalous visible light response in organolead bromide perovskite*. Journal of the American Chemical Society, 2015. **137**(34): p. 11144-11149.
50. Jiang, S., et al., *Pressure-Dependent Polymorphism and Band-Gap Tuning of*

- Methylammonium Lead Iodide Perovskite*. *Angewandte Chemie*, 2016. **128**(22): p. 6650-6654.
51. Ong, K.P., et al., *Structural evolution in methylammonium lead iodide CH₃NH₃PbI₃*. *The Journal of Physical Chemistry A*, 2015. **119**(44): p. 11033-11038.
 52. Szafraniecki, M. and A. Katrusiak, *Mechanism of Pressure-Induced Phase Transitions, Amorphization, and Absorption-Edge Shift in Photovoltaic Methylammonium Lead Iodide*. *The Journal of Physical Chemistry Letters*, 2016. **7**(17): p. 3458-3466.
 53. Knop, O., et al., *Alkylammonium lead halides. Part 2. CH₃NH₃PbX₃ (X= Cl, Br, I) perovskites: cuboctahedral halide cages with isotropic cation reorientation*. *Canadian Journal of Chemistry*, 1990. **68**(3): p. 412-422.
 54. Slavney, A.H., et al., *Chemical approaches to addressing the instability and toxicity of lead-halide perovskite absorbers*. *Inorganic chemistry*, 2017. **56**(1): p. 46-55.
 55. Hao, F., et al., *Lead-free solid-state organic-inorganic halide perovskite solar cells*. *Nature photonics*, 2014. **8**(6): p. 489-494.
 56. Sabba, D., et al., *Impact of anionic Br-substitution on open circuit voltage in lead free perovskite (CsSnI_{3-x}Br_x) solar cells*. *The Journal of Physical Chemistry C*, 2015. **119**(4): p. 1763-1767.
 57. Sun, Y.-Y., et al., *Chalcogenide perovskites for photovoltaics*. *Nano letters*, 2015. **15**(1): p. 581-585.
 58. Repins, I., et al., *19.9%-efficient ZnO/CdS/CuInGaSe₂ solar cell with 81.2% fill factor*. *Progress in Photovoltaics: Research and applications*, 2008. **16**(3): p. 235-239.
 59. Wang, C., et al., *Design of I₂-II-IV-VI₄ semiconductors through element substitution: the thermodynamic stability limit and chemical trend*. *Chemistry of Materials*, 2014. **26**(11): p. 3411-3417.
 60. Grinberg, I., et al., *Perovskite oxides for visible-light-absorbing ferroelectric and photovoltaic materials*. *Nature*, 2013. **503**(7477): p. 509-512.
 61. Balaz, S., et al., *Electronic structure of tantalum oxynitride perovskite photocatalysts*. *Chemistry of Materials*, 2013. **25**(16): p. 3337-3343.
 62. Schoop, L.M., et al., *Lone pair effect, structural distortions, and potential for superconductivity in Tl perovskites*. *Inorganic chemistry*, 2013. **52**(9): p. 5479-5483.

63. Sun, Y.-Y., et al., *Discovering lead-free perovskite solar materials with a split-anion approach*. *Nanoscale*, 2016. **8**(12): p. 6284-6289.
64. Hohenberg, P. and W. Kohn, *Inhomogeneous electron gas*. *Physical review*, 1964. **136**(3B): p. B864.
65. Goodfellow, I., Y. Bengio, and A. Courville, *Deep learning*. 2016: MIT press.
66. Born, M. and R. Oppenheimer, *Zur quantentheorie der molekeln*. *Annalen der physik*, 1927. **389**(20): p. 457-484.
67. Hartree, D.R. *The wave mechanics of an atom with a non-Coulomb central field. Part I. Theory and methods*. in *Mathematical Proceedings of the Cambridge Philosophical Society*. 1928. Cambridge university press.
68. Fock, V., *Näherungsmethode zur Lösung des quantenmechanischen Mehrkörperproblems*. *Zeitschrift für Physik*, 1930. **61**(1-2): p. 126-148.
69. Jones, R.O. and O. Gunnarsson, *The density functional formalism, its applications and prospects*. *Reviews of Modern Physics*, 1989. **61**(3): p. 689.
70. Kohn, W. and L.J. Sham, *Self-consistent equations including exchange and correlation effects*. *Physical review*, 1965. **140**(4A): p. A1133.
71. Dirac, P.A. *Note on exchange phenomena in the Thomas atom*. in *Mathematical proceedings of the Cambridge philosophical society*. 1930. Cambridge University Press.
72. Hubbard, J., *The description of collective motions in terms of many-body perturbation theory. II. The correlation energy of a free-electron gas*. *Proceedings of the Royal Society of London. Series A. Mathematical and Physical Sciences*, 1958. **243**(1234): p. 336-352.
73. Gell-Mann, M. and K.A. Brueckner, *Correlation energy of an electron gas at high density*. *Physical Review*, 1957. **106**(2): p. 364.
74. Carr Jr, W. and A. Maradudin, *Ground-state energy of a high-density electron gas*. *Physical Review*, 1964. **133**(2A): p. A371.
75. Wigner, E., *On the interaction of electrons in metals*. *Physical Review*, 1934. **46**(11): p. 1002.
76. Perdew, J.P. and A. Zunger, *Self-interaction correction to density-functional approximations for many-electron systems*. *Physical Review B*, 1981. **23**(10): p. 5048-5079.
77. Ceperley, D.M. and B.J. Alder, *Ground state of the electron gas by a stochastic method*.

- Physical review letters, 1980. **45**(7): p. 566.
78. Pfrommer, B.G., et al., *Relaxation of crystals with the quasi-Newton method*. Journal of Computational Physics, 1997. **131**(1): p. 233-240.
79. Hellmann, H., *Einführung in die Quantenchemie (Deuicke, Leipzig); Feynman RP 1939*. Phys. Rev, 1937. **56**: p. 340.
80. Feynman, R.P., *Forces in molecules*. Physical review, 1939. **56**(4): p. 340.
81. Van De Walle, A., M. Asta, and G. Ceder, *The alloy theoretic automated toolkit: A user guide*. Calphad, 2002. **26**(4): p. 539-553.
82. Connolly, J. and A. Williams, *Density-functional theory applied to phase transformations in transition-metal alloys*. Physical Review B, 1983. **27**(8): p. 5169.
83. Kamerlingh Onnes, H., *The resistance of pure mercury at helium temperatures*. Commun. Phys. Lab. Univ. Leiden, b, 1911. **120**.
84. Ashcroft, N.W. and N.D. Mermin, *Solid state physics*. 1976, holt, rinehart and winston, new york London.
85. Maxwell, E., *Isotope effect in the superconductivity of mercury*. Physical Review, 1950. **78**(4): p. 477.
86. McMillan, W., *Transition temperature of strong-coupled superconductors*. Physical Review, 1968. **167**(2): p. 331.
87. Ambegaokar, V. and L. Tewordt, *Theory of the electronic thermal conductivity of superconductors with strong electron-phonon coupling*. Physical Review, 1964. **134**(4A): p. A805.
88. Morel, P. and P. Anderson, *Calculation of the superconducting state parameters with retarded electron-phonon interaction*. Physical Review, 1962. **125**(4): p. 1263.
89. Johannes, M. and I. Mazin, *Fermi surface nesting and the origin of charge density waves in metals*. Physical Review B, 2008. **77**(16): p. 165135.
90. Allen, P.B., *Handbook of Superconductivity*. New York: Academic, 1999: p. 478.
91. Allen, P.B. and R. Dynes, *Transition temperature of strong-coupled superconductors reanalyzed*. Physical Review B, 1975. **12**(3): p. 905.
92. Eliashberg, G., *Interactions between electrons and lattice vibrations in a superconductor*. Sov. Phys. JETP, 1960. **11**(3): p. 696-702.

93. Eisenschitz, R. and F. London, *Über das Verhältnis der van der Waalsschen Kräfte zu den homöopolaren Bindungskräften*. Zeitschrift für Physik, 1930. **60**(7-8): p. 491-527.
94. Kittel, C., *Introduction to solid state physics*. 1976.
95. Lennard-Jones, J.E., *Cohesion*. Proceedings of the Physical Society, 1931. **43**(5): p. 461-482.
96. Rydberg, H., et al., *Hard numbers on soft matter*. Surface science, 2003. **532**: p. 606-610.
97. Berland, K., et al., *van der Waals forces in density functional theory: a review of the vdW-DF method*. Reports on Progress in Physics, 2015. **78**(6): p. 066501.
98. Zhang, Y. and W. Yang, *Comment on "Generalized gradient approximation made simple"*. Physical Review Letters, 1998. **80**(4): p. 890.
99. Lee, K., et al., *Higher-accuracy van der Waals density functional*. Physical Review B, 2010. **82**(8): p. 081101.
100. Hamada, I., *van der Waals density functional made accurate*. Physical Review B, 2014. **89**(12): p. 121103.
101. Hamada, I., *Erratum: van der Waals density functional made accurate [Phys. Rev. B 89, 121103 (r)(2014)]*. Physical Review B, 2015. **91**(11): p. 119902.
102. Berland, K. and P. Hyldgaard, *Exchange functional that tests the robustness of the plasmon description of the van der Waals density functional*. Physical Review B, 2014. **89**(3): p. 035412.
103. Klimeš, J., D.R. Bowler, and A. Michaelides, *Van der Waals density functionals applied to solids*. Physical Review B, 2011. **83**(19): p. 195131.
104. Sabatini, R., T. Gorni, and S. De Gironcoli, *Nonlocal van der Waals density functional made simple and efficient*. Physical Review B, 2013. **87**(4): p. 041108.
105. Vydrov, O.A. and T. Van Voorhis, *Nonlocal van der Waals density functional: The simpler the better*. The Journal of chemical physics, 2010. **133**(24): p. 244103.
106. Thomas, L.H., *The motion of the spinning electron*. Nature, 1926. **117**(2945): p. 514-514.
107. Wang, H. and B. Raj, *On the origin of deep learning*. arXiv preprint arXiv:1702.07800, 2017.
108. Hornik, K., *Approximation capabilities of multilayer feedforward networks*. Neural networks, 1991. **4**(2): p. 251-257.

109. Giannozzi, P., et al., *QUANTUM ESPRESSO: a modular and open-source software project for quantum simulations of materials*. Journal of physics: Condensed matter, 2009. **21**(39): p. 395502.
110. Ryan, D.P., C.C. Compton, and R.J. Mayer, *Carcinoma of the anal canal*. New England Journal of Medicine, 2000. **342**(11): p. 792-800.
111. Perini, A., G. Jacucci, and G. Martin, *Cluster free energy in the simple-cubic Ising model*. Physical Review B, 1984. **29**(5): p. 2689.
112. van de Walle, A. and G. Ceder, *Automating first-principles phase diagram calculations*. Journal of Phase Equilibria, 2002. **23**(4): p. 348-359.
113. Head, J.D. and M.C. Zerner, *A Broyden—Fletcher—Goldfarb—Shanno optimization procedure for molecular geometries*. Chemical physics letters, 1985. **122**(3): p. 264-270.
114. Perdew, J.P., K. Burke, and M. Ernzerhof, *Generalized gradient approximation made simple*. Physical review letters, 1996. **77**(18): p. 3865.
115. Methfessel, M. and A. Paxton, *High-precision sampling for Brillouin-zone integration in metals*. Physical Review B, 1989. **40**(6): p. 3616.
116. Setyawan, W. and S. Curtarolo, *High-throughput electronic band structure calculations: Challenges and tools*. Computational materials science, 2010. **49**(2): p. 299-312.
117. Quan, Y., S.S. Ghosh, and W.E. Pickett, *Compressed hydrides as metallic hydrogen superconductors*. Physical Review B, 2019. **100**(18): p. 184505.
118. Pinsook, U., *In search for near-room-temperature superconducting critical temperature of metal superhydrides under high pressure: A review*. Journal of Metals, Materials and Minerals, 2020. **30**(2).
119. Ma, Y., et al., *Prediction of superconducting ternary hydride MgGeH 6: from divergent high-pressure formation routes*. Physical Chemistry Chemical Physics, 2017. **19**(40): p. 27406-27412.
120. Liang, X., et al., *Potential high-T c superconductivity in CaYH 12 under pressure*. Physical Review B, 2019. **99**(10): p. 100505.
121. Monkhorst, H.J. and J.D. Pack, *Special points for Brillouin-zone integrations*. Physical review B, 1976. **13**(12): p. 5188.
122. Perdew, J.P., et al., *Restoring the density-gradient expansion for exchange in solids and*

- surfaces*. Physical review letters, 2008. **100**(13): p. 136406.
123. Dion, M., et al., *Van der Waals density functional for general geometries*. Physical review letters, 2004. **92**(24): p. 246401.
124. Thonhauser, T., et al., *Spin signature of nonlocal correlation binding in metal-organic frameworks*. Physical review letters, 2015. **115**(13): p. 136402.
125. Govinda, S., et al., *Is CH₃NH₃PbI₃ Polar*. J. Phys. Chem. Lett, 2016. **7**(13): p. 2412-2419.
126. Chen, T., et al., *Rotational dynamics of organic cations in the CH₃NH₃PbI₃ perovskite*. Physical Chemistry Chemical Physics, 2015. **17**(46): p. 31278-31286.
127. Li, J. and P. Rinke, *Atomic structure of metal-halide perovskites from first principles: The chicken-and-egg paradox of the organic-inorganic interaction*. Physical Review B, 2016. **94**(4): p. 045201.
128. Vitos, L., et al., *The surface energy of metals*. Surface science, 1998. **411**(1-2): p. 186-202.
129. Ropo, M., K. Kokko, and L. Vitos, *Assessing the Perdew-Burke-Ernzerhof exchange-correlation density functional revised for metallic bulk and surface systems*. Physical Review B, 2008. **77**(19): p. 195445.
130. Tao, J., et al., *Climbing the density functional ladder: Nonempirical meta-generalized gradient approximation designed for molecules and solids*. Physical Review Letters, 2003. **91**(14): p. 146401.
131. Langreth, D.C. and S. Vosko, *Response functions and nonlocal approximations*, in *Advances in quantum chemistry*. 1990, Elsevier. p. 175-199.
132. Elliott, P. and K. Burke, *Non-empirical derivation of the parameter in the B88 exchange functional*. Canadian Journal of Chemistry, 2009. **87**(10): p. 1485-1491.
133. Birch, F., *Finite elastic strain of cubic crystals*. Physical review, 1947. **71**(11): p. 809.
134. Onoda-Yamamuro, N., T. Matsuo, and H. Suga, *Calorimetric and IR spectroscopic studies of phase transitions in methylammonium trihalogenoplumbates (II)*. Journal of Physics and Chemistry of Solids, 1990. **51**(12): p. 1383-1395.
135. Capitani, F., et al., *Locking of Methylammonium by Pressure-Enhanced H-Bonding in (CH₃NH₃)PbBr₃ Hybrid Perovskite*. The Journal of Physical Chemistry C, 2017. **121**(50): p. 28125-28131.

136. Ghosh, D., et al., *Good Vibrations: Locking of Octahedral Tilting in Mixed-Cation Iodide Perovskites for Solar Cells*. ACS Energy Letters, 2017. **2**(10): p. 2424-2429.
137. Kresse, G. and J. Furthmüller, *Phys. Rev. B: Condens. Matter Mater. Phys.* 1996.
138. Hobbs, D., G. Kresse, and J. Hafner, *Fully unconstrained noncollinear magnetism within the projector augmented-wave method*. Physical Review B, 2000. **62**(17): p. 11556.
139. Ehrlich, S., et al., *System-dependent dispersion coefficients for the DFT-D3 treatment of adsorption processes on ionic surfaces*. ChemPhysChem, 2011. **12**(17): p. 3414-3420.
140. Hunter, J.D., *Matplotlib: A 2D graphics environment*. Computing in science & engineering, 2007. **9**(03): p. 90-95.
141. Momma, K. and F. Izumi, *VESTA 3 for three-dimensional visualization of crystal, volumetric and morphology data*. Journal of applied crystallography, 2011. **44**(6): p. 1272-1276.
142. Sukmas, W., et al., *Preferred oriented cation configurations in high pressure phases IV and V of methylammonium lead iodide perovskite*. Scientific reports, 2020. **10**(1): p. 1-8.
143. Fabini, D.H., et al., *Universal dynamics of molecular reorientation in hybrid lead iodide perovskites*. Journal of the American Chemical Society, 2017. **139**(46): p. 16875-16884.
144. Abadi, M., et al., *Tensorflow: Large-scale machine learning on heterogeneous distributed systems*. arXiv preprint arXiv:1603.04467, 2016.
145. Saidi, W.A., W. Shadid, and I.E. Castelli, *Machine-learning structural and electronic properties of metal halide perovskites using a hierarchical convolutional neural network*. npj Computational Materials, 2020. **6**(1): p. 1-7.
146. Kingma, D.P. and J. Ba, *Adam: A method for stochastic optimization*. arXiv preprint arXiv:1412.6980, 2014.
147. Yamada, Y., et al., *Optical properties of switchable mirrors based on magnesium-calcium alloy thin films*. Applied Physics Letters, 2009. **94**(19): p. 191910.
148. Bertheville, B. and K. Yvon, *Ca19Mg8H54, a new salt-like ternary metal hydride*. Journal of alloys and compounds, 1999. **290**(1-2): p. L8-L10.
149. Perdew, J.P., *Accurate density functional for the energy: Real-space cutoff of the gradient expansion for the exchange hole*. Physical Review Letters, 1985. **55**(16): p. 1665.
150. Perdew, J.P., P. Ziesche, and H. Eschrig, *Electronic structure of solids ' 91*. 1991, Akademie

Verlag, Berlin.

151. Perdew, J.P., et al., *Erratum: Atoms, molecules, solids, and surfaces: Applications of the generalized gradient approximation for exchange and correlation*. Physical Review B, 1993. **48**(7): p. 4978.
152. Perdew, J.P. and Y. Wang, *Erratum: Accurate and simple analytic representation of the electron-gas correlation energy [Phys. Rev. B 45, 13244 (1992)]*. Physical Review B, 2018. **98**(7): p. 079904.
153. Rasolt, M. and D. Geldart, *Exchange and correlation energy in a nonuniform fermion fluid*. Physical Review B, 1986. **34**(2): p. 1325.
154. Langreth, D.C. and M. Mehl, *Beyond the local-density approximation in calculations of ground-state electronic properties*. Physical Review B, 1983. **28**(4): p. 1809.
155. Krieger, J., Y. Li, and G. Iafate, *Derivation and application of an accurate Kohn-Sham potential with integer discontinuity*. Physics Letters A, 1990. **146**(5): p. 256-260.



จุฬาลงกรณ์มหาวิทยาลัย
CHULALONGKORN UNIVERSITY

VITA

NAME Wiwittawin Sukmas

DATE OF BIRTH 6 October 1994

PLACE OF BIRTH Bangkok, Thailand

INSTITUTIONS ATTENDED Chulalongkorn University

HOME ADDRESS 6/6 M.2 Samrongklang Phrapradaeng Samutprakarn 10130

PUBLICATION

- o Sukmas, W., Sakulsupich, V., Tsuppayakorn-Aek, P., Pinsook, U., Pakornchote, T., Klinkla, R., & Bovornratanaraks, T. (2020). Preferred oriented cation configurations in high pressure phases IV and V of methylammonium lead iodide perovskite. *Scientific reports*, 10(1), 1-8.
- o Sukmas, W., Tsuppayakorn-ae, P., Pinsook, U., & Bovornratanaraks, T. (2020). Near-room-temperature superconductivity of Mg/Ca substituted metal hexahydride under pressure. *Journal of Alloys and Compounds*, 849, 156434.
- o Sukmas, W., Pinsook, U., Tsuppayakorn-ae, P., Pakornchote, T., Sukserm, A., & Bovornratanaraks, T. (2019). Organic Molecule Orientations and Rashba–Dresselhaus Effect in α -Formamidinium Lead Iodide. *The Journal of Physical Chemistry C*, 123(27), 16508-16515.
- o Sukmas, W., Nedkun, P., Pinsook, U., Tsuppayakorn-ae, P., & Bovornratanaraks, T. (2019, November). Effect of formamidinium cation on electronic structure of formamidinium lead iodide. In *Journal of Physics: Conference Series* (Vol. 1380, No. 1, p. 012080). IOP Publishing.
- o Sukmas, W., Ektarawong, A., Tsuppayakorn-ae, P., Alling, B., Pinsook, U., & Bovornratanaraks, T. (2021). Data-

Driven Analyses of Rotational Energy-landscapes of Organic Cation in Substituted Alloy Perovskite. *Materials Advances*.

o Tsuppayakorn-Aek, P., Sukmas, W., Ahuja, R., Luo, W., & Bovornratanaraks, T. (2021). Stabilization and electronic topological transition of hydrogen-rich metal Li 5 MoH 11 under high pressures from first-principles predictions. *Scientific Reports*, 11(1), 1-10.

o Chintananon, N., Tsuppayakorn-aeK, P., Sukmas, W., Bovornratanaraks, T., & Pinsook, U. (2021). Effects of Mg substitution on electronic properties of CaF₂. In *Journal of Physics: Conference Series* (Vol. 1719, No. 1, p. 012027). IOP Publishing.

o Thatribud, A., Rassamesard, A., Sukmas, W., & Pinsook, U. (2021). Effect of lattice polarisability in optical properties of methylammonium lead iodide by modified Becke-Johnson functionals and Bethe-Salpeter equation. *Computational Materials Science*, 189, 110245.

o Pluengphon, P., Tsuppayakorn-aeK, P., Sukmas, W., Inceesungvorn, B., & Bovornratanaraks, T. (2021). Dynamical stabilization and H-vacancy diffusion kinetics of lightweight complex hydrides: Ab initio study for hydrogen storage improvement. *International Journal of Hydrogen Energy*.

o Sukmas, W., Tsuppayakorn-aeK, P., Pinsook, U., & Bovornratanaraks, T. (2020). Near-room-temperature superconductivity of Mg/Ca substituted metal hexahydride under pressure. *Journal of Alloys and Compounds*, 849, 156434.

o Sukmas, W., Pinsook, U., Tsuppayakorn-aeK, P., Pakornchote, T., Sukserm, A., & Bovornratanaraks, T. (2019). Organic Molecule Orientations and Rashba–Dresselhaus Effect in α -Formamidinium Lead Iodide. *The Journal of Physical*

Chemistry C, 123(27), 16508-16515.

o Sukmas, W., Nedkun, P., Pinsook, U., Tsuppayakorn-ae, P., & Bovornratanaraks, T. (2019, November). Effect of formamidinium cation on electronic structure of formamidinium lead iodide. In *Journal of Physics: Conference Series* (Vol. 1380, No. 1, p. 012080). IOP Publishing.

o Sukmas, W., Ektarawong, A., Tsuppayakorn-ae, P., Alling, B., Pinsook, U., & Bovornratanaraks, T. Data-Driven Analyses of Rotational Energy-landscapes of Organic Cation in Substituted Alloy Perovskite— Just accepted

o Tsuppayakorn-Aek, P., Sukmas, W., Ahuja, R., Luo, W., & Bovornratanaraks, T. (2021). Stabilization and electronic topological transition of hydrogen-rich metal Li₅MoH₁₁ under high pressures from first-principles predictions. *Scientific Reports*, 11(1), 1-10.

o Chintananon, N., Tsuppayakorn-ae, P., Sukmas, W., Bovornratanaraks, T., & Pinsook, U. (2021). Effects of Mg substitution on electronic properties of CaF₂. In *Journal of Physics: Conference Series* (Vol. 1719, No. 1, p. 012027). IOP Publishing.

o Thatribud, A., Rassamesard, A., Sukmas, W., & Pinsook, U. (2021). Effect of lattice polarisability in optical properties of methylammonium lead iodide by modified Becke-Johnson functionals and Bethe-Salpeter equation. *Computational Materials Science*, 189, 110245.